ORNL/TM-2020/1471

Second Annual Progress Report on Correlation between Microstructure and Mechanical Properties of Neutron-Irradiated Ferritic-Martensitic and Austenitic Steels

Weicheng Zhong
Lizhen Tan
Oak Ridge National Laboratory

February 28, 2020

OAK RIDGE NATIONAL LABORATORY
MANAGED BY UT-BATTELLE FOR THE US DEPARTMENT OF ENERGY

ORNL/TM-2020/1471
M2NA-17OR0204018

FY 2017 Consolidated Innovative Nuclear Research (CINR)
Nuclear Science User Facilities (NSUF)
Light Water Reactor Sustainability (LWRS)

SECOND ANNUAL PROGRESS REPORT ON CORRELATION BETWEEN MICROSTRUCTURE AND MECHANICAL PROPERTIES OF NEUTRON-IRRADIATED FERRITIC-MARTENSITIC AND AUSTENITIC STEELS

Weicheng Zhong, and Lizhen Tan
Oak Ridge National Laboratory

Date Published: February 28, 2020

Prepared by
OAK RIDGE NATIONAL LABORATORY
Oak Ridge, TN 37831-6283
managed by
UT-BATTELLE, LLC
for the
US DEPARTMENT OF ENERGY
under contract DE-AC05-00OR22725

CONTENTS

LIST OF TABLES

LIST OF FIGURES

ACKNOWLEDGMENTS

This research was sponsored by the U.S. Department of Energy (DOE), Office of Nuclear Energy (NE), the FY 2017 Consolidated Innovative Nuclear Research (CINR) Nuclear Science User Facilities (NSUF) program and the Light Water Reactor Sustainability (LWRS) program. The authors are grateful to Kory Linton of ORNL, Collin Knight of Idaho National Laboratory, and Tarik Saleh of Los Alamos National Laboratory for shipping the identified samples and providing essential support on the access to the LAMDA facilities through the NSUF program. We also thank Patricia Tedder, Stephanie Curlin, James Dixon, Brandon Hambrick and Joshua Schmidlin of ORNL for sample reception, preparation, and hardness measurements. T.S. Byun and Omer Karakoc of ORNL are appreciated for technical review of this report.

EXECUTIVE SUMMARY

Ferritic-martensitic steels G92-2b (an optimized Grade 92 heat), NF616 and T91, and austenitic stainless steel 800H and its Grain Boundary Engineering (GBE)-treated version 800H-TMP (ThermoMechanical Processing) were irradiated in the High Flux Isotope Reactor (HFIR) of Oak Ridge National Laboratory (ORNL) and the Advanced Test Reactor (ATR) of Idaho National Laboratory (INL). Selected G92-2b samples were irradiated up to 14.66 dpa in the HFIR at two temperature ranges: 400–496.7℃ and 683.3–720℃. NF616 and T91 were irradiated in the ATR up to 8.16 dpa with the irradiation temperatures ranged from 241℃ to 447.5℃. Alloy 800H and 800H-TMP samples were irradiated in both the HFIR and the ATR. Selected 800H and 800H-TMP samples had HFIR irradiation to 1.28 dpa at 580℃ and ATR irradiation up to 9.12 dpa at 359℃ to 431℃. Vickers hardness measurements, fractography, and microstructural characterization were performed on the selected samples in the Low Activation Materials Design and Analysis (LAMDA) laboratory.

Radiation-hardening of G92-2b was observed at the lower doses and lower irradiation temperatures (400-496.7℃), with GB03 (0.52 dpa at 400℃) and GB04 (7.44 dpa at ~490℃) showing ~12% and ~8% hardening, respectively. Softening by ~14% was observed for GB05 (14.66 dpa at 496.7℃). Radiation-softening of G92-2b was more prevalent at the higher irradiation temperatures (683.3-~720℃), with GB10 (0.46 dpa at 683.3℃), GB11 (7.44 dpa at ~720℃), and GB12 (14.63 dpa at ~720℃) showing ~8%, ~8%, and ~40% softening, respectively. Radiation-hardening of NF616 and T91 was observed with the hardness increased by ~37% to ~65% depending on the irradiation doses and irradiation temperatures. Within the studied irradiation conditions of NF616 and T91, samples with a higher dose had a larger hardness after irradiation. All the tested alloy 800H and 800H-TMP samples in this work showed radiation-hardening by ~96±7% to ~152±10%. Alloy 800H-TMP tended to have slightly smaller radiation-hardening than alloy 800H.

The fractography results of G92-2b sample GB03, GB10, and GB11, together with the previously characterized fractography of GB04, GB05, and GB12, indicated that the ductility of G92-2b was maintained up to 14.66 dpa at the lower irradiation temperatures of 400-496.7℃, while some loss of ductility (less necking) was observed for higher doses at the higher irradiation temperatures of 683.3-720℃. This agrees with the previously reported tensile test results of G92-2b, where the elongation of G92-2b was reduced at higher doses at the higher irradiation temperatures. Dimple sizes increased at higher doses, which are more evident at the higher irradiation temperatures of 683.3-~720℃. The fractography of NF616 sample D2 (2.96 dpa at 291.5℃), D4 (5.91 dpa at 359℃), and D6 (8.16 dpa at 431℃) indicated loss of ductility with negligible necking for sample D2, while ductile failure for samples D4 and D6. Fractography of alloy 800H and 800H-TMP samples in various irradiation conditions showed ductile failure with obvious necking. Dimples were observed, with some of them containing large Ti-rich particles, in all the 800H/800H-TMP samples.

Electron backscatter diffraction characterization of GB12 indicated the recovery of the lath structure, which was generally replaced by an equiaxed grain structure. Transmission electron microscopy (TEM) characterization showed the presence of frequent $M_{23}C_6$ (M = primarily Cr), MX (M = primarily V), spherical Nb(C,N) precipitates, and occasional Laves phase precipitates in the G92-2b samples. MX precipitates with sizes of 20-30 nm were observed at boundaries of smaller grains, indicating the pinning effect of the V-rich precipitates. The lath structure recovery was more evident at the higher irradiation temperatures (683.3-~720℃), with decreased densities of line dislocations and $M_{23}C_6$ precipitates. The irradiated T91 (TA04) showed the growth of $M_{23}C_6$ precipitates to 101 ± 40 nm from the initial 68 ± 22 nm in the unirradiated condition. Dislocation loops of both {100} and {111} types were present in TA04. TEM characterization was also performed on the irradiated 800H (N4, N5, N6, and AR2) and 800H-TMP (P4, P5, P6, and HG1). Accumulation of $M_{23}C_6$ precipitates at grain boundaries was observed in all the

800H/800H-TMP samples, and the presence of Ti(C,N) precipitates at grain boundaries and in the matrix was observed in the irradiated 800H-TMP. Some Ti(C,N) precipitates are embedded in the $M_{23}C_6$ precipitates, maintaining specific orientation relationships between the precipitates and between the precipitate and matrix. In addition, nanoscale Si-rich clusters were observed in the matrix of all the 800H/800H-TMP samples, with EDS Si maps tending to have a lower contrast in 800H-TMP samples. Atom probe tomography was conducted on the same samples, supported by a Rapid Turnaround Examination project under Nuclear Science User Facilities. The results are being analyzed to be integrated with the TEM results for a confident description of the γ' precipitates. Dislocation loops also formed in all the 800H/800H-TMP samples. The density and the average size of dislocation loops were quantified to be in the order of $10^{22} – 10^{23}$ m^{-3} and 11.7 – 15.9 nm, respectively, in the ATR-irradiated 800H/800H-TMP samples. The loop densities in irradiated 800H were higher than that in irradiated 800H-TMP under the same irradiation conditions.

Further systematic data analyses, together with some complementary experiments, will be pursued for these samples to foster peer-reviewed journal article publications.

1. INTRODUCTION

Advanced alloys are desired to provide greater safety margins, design flexibility and economics compared to traditional reactor materials. Ferritic-martensitic steel Grade 92 and austenitic Alloy 800/800H are two of the promising alloys interested by the current Advanced Radiation-Resistant Materials (ARRM) and Light Water Reactor Sustainability (LWRS) programs. However, systematic studies on neutron-irradiation induced changes in microstructures and mechanical properties are deficient for the alloys. The objective of this project is to develop correlations between microstructures and mechanical properties of the neutron-irradiated Grade 92 and Alloy 800/800H, based on the experimental results generated from this work. It is expected to develop broader correlations for these types of steels by comparing the results of this work with that of similar alloys such as Grade 91, Alloy 709 and type 304/316 stainless steels from literature and the ongoing studies, with the aid of thermodynamics, kinetics, and microstructural hardening modeling.

Samples of Grade 92 and Alloy 800H selected in this work were primarily irradiated in two test reactors for up to ~14 displacements per atom (dpa) at ~241–720°C. Samples of Grade 91, irradiated in the same reactors, were selected as references of Grade 92. Few samples from other two reactors will be included for comparison. Both irradiated and unirradiated samples from the same heat of the materials will be examined to elucidate the radiation-induced evolutions in microstructures, mechanical properties, and deformation mechanisms. To be more specific, mechanical properties such as tensile properties, modulus, hardness, and viscoplasticity will be measured through tensile, Vickers hardness and nanoindentation tests. Microstructural characterization of the samples will be carried out using the state-of-the-art instruments and techniques provided through the Nuclear Science User Facilities (NSUF). The obtained experimental results will then be used to establish the knowledgebase on the effects of alloy chemistry, thermomechanical-processing, and irradiation conditions on microstructures and mechanical properties of Grade 92 and Alloy 800H.

Outcomes of this project will include a comprehensive set of data including microstructures and mechanical properties of both irradiated and unirradiated samples of the interested steels, which will not only help understanding the essential performance of similar alloys, but more importantly to gain indispensable insights into the development of advanced alloys with superior radiation resistance. The outcomes can also serve as inputs and/or benchmarks for microstructural and mechanical property modeling of irradiated ferritic-martensitic and austenitic steels. The accomplishment of this project will directly benefit the LWRS program and bring value to the Advanced Reactor Technologies and Small Modular Reactors programs.

Samples irradiated in the High Flux Isotope Reactor (HFIR) of Oak Ridge National Laboratory (ORNL) and Advanced Test Reactor (ATR) of Idaho National Laboratory (INL) have been performed tensile tested, and the result have been reported [1] [2] [3]. Hardness measurement and the microstructure characterization have been performed on the samples. This report summarizes the post-irradiation examination results of the selected ORNL, LANL (Los Alamos National Laboratory), and INL samples.

2. SELECTED SAMPLES

2.1 ORNL SAMPLES

The selected ORNL samples include G92-2b and 800H samples irradiated to 0.46–14.66 dpa at 400 to ~720°C in the HFIR, which are listed in Table 1, together with the alloy compositions in

Table 2. The G92-2b is a heat of optimized Grade 92, which was developed under the Advanced Reactor Technologies (ART) program [4]. It showed the improved strength and creep resistance compared with conventional Grade 92 such as NF616. The AR2 and HG1 samples are Incoloy 800H samples in a commercial solution-annealed condition and a thermomechanical processing (TMP) condition, respectively. The G92-2b samples are type SS-J2 miniature tensile specimens with 16 × 4 × 0.51 mm overall size and 5 × 1.2 × 0.51 mm for the gauge section. The 800H and 800H-TMP samples are in type SS-3 miniature tensile specimens with 25.4 × 4.95 × 0.76 mm overall size and 7.62 × 1.52 × 0.76 mm for the gauge section.

G92-2b was normalized at 1080°C for 1 h, followed by hot-rolling to 0.6"-thick plate from 1" at 1080°C and water quenched, and tempered at 750°C for 2 h with air cooling. The 800H was solution-annealed at 1177°C for 24 minutes per centimeter of thickness, followed by a water quench. The 800H-TMP was based on the 800H, subjected to ~6.6% thickness reduction by rolling at room temperature and then annealed at 1050°C for 1.5 h with water quench. The TMP led to a grain boundary engineering (GBE) effect to significantly increase the fraction of low-Σ coincidence site lattice (CSL) boundaries, e.g., nearly 70% (800H-TMP) vs. ~40% (800H) low-Σ CSL boundaries [5]. GBE with a significantly increased fraction of low-Σ CSL boundaries would benefit a variety of properties such as strength and resistance to creep, stress corrosion cracking, and oxidation [6]. The 800H-TMP exhibited noticeable enhancements in the resistance to thermal aging [7] and corrosion in supercritical water and high-temperature air [8] [9] [10] [11]. Preliminary studies also showed some improvements in resistance to neutron irradiation [12] [13]. Therefore, the pair of 800H/800H-TMP samples were irradiated in a nearly identical condition to elucidate the beneficial effects of GBE/TMP on the neutron irradiation resistance of 800H.

Table 1. Irradiation condition of ORNL HFIR-irradiated samples.

Specimen type	Alloy	Sample ID	Temperature (℃)	Dose (dpa)	Irradiation time (days)
SS-J2	G92-2b	GB03	400	0.52	10
		GB04	~490	7.44	126
		GB05	496.7	14.66	228
		GB10	683.3	0.46	7
		GB11	~720	7.44	125
		GB12	~720	14.63	202
SS-3	800H	AR2	580	1.28	23.3
	800H-TMP	HG1			

Table 2. Compositions in weight percent (wt%) of the HFIR samples, with Fe as balance.

Alloy	Cr	Ni	Mn	Si	Ti	V	W	Mo	Nb	Cu	C	N	P	S	B
G92-2b	8.9	0.1	0.47	0.14		0.23	1.9	0.43	0.11		0.087	0.045			< 0.002
800H/800H-TMP	20.42	31.59	0.76	0.57	0.5					0.42	0.069		0.014	0.001	

2.2 IRRADIATION CONDITIONS

Some of the irradiation temperatures are reported according to the analyzed results of the accompanied SiC temperature monitor samples irradiated with the selected samples, while the approximate irradiation temperatures with a "~" sign in Table 1 are estimated from extrapolation according to the available SiC temperature monitor results. Figure 1 shows the analyzed temperature from the available SiC temperature monitor samples in the same irradiation campaign as a function of irradiation dose in a logarithmic scale. Each dose has three temperature data points from the SiC samples at the top, middle, and bottom sections of irradiation capsules, which are not differentiated in the plot. The bottom section had relatively stable temperatures, while the top section had relatively large variations with increasing doses. The middle section generally had the highest temperatures, especially at higher doses.

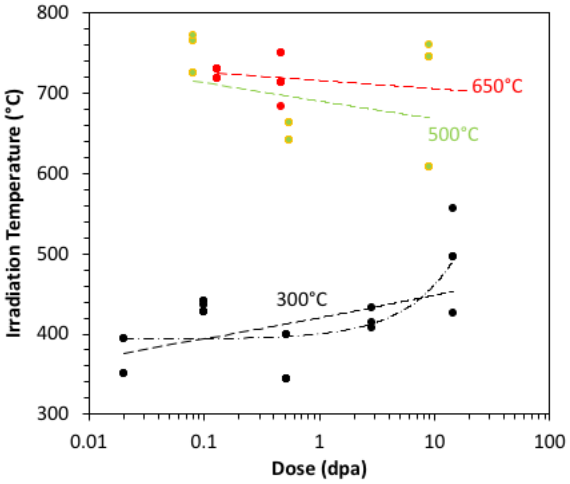

Figure 1. Irradiation temperature as a function of dose of steel samples irradiated with the G92-2b samples.

The dose-dependent irradiation temperature data are roughly fitted with a power function as shown in dashed lines in Figure 1, while the 300°C data also exhibited a better fitting by a linear function as shown in a dash-dot line. In general, the planned 300°C irradiation turns out to be above ~350°C and increasing with higher doses, especially for doses above 3 dpa. In contrast, the planned 500 and 650°C irradiations had similar irradiation temperatures above 600°C, tending to slightly decrease with increasing doses. According to Figure 1, it is expected that GB04 at the middle section of the irradiation capsule were irradiated at ~490°C, while GB11 and GB12 at the middle section of the irradiation capsule was irradiated at ~720°C. The irradiation temperatures were ~100–200°C and ~30–70°C higher than the planned 300 and 650°C. One of the factors causing such large increases from the planned temperatures would be gamma heat generated from tungsten samples that were irradiated with the steel samples in the same capsules. The selected Grade 92 samples irradiated in the Advanced Test Reactor (ATR) of Idaho National laboratory were irradiated at temperatures in the range of 241–431°C, which will provide low-temperature properties to have an overall picture about radiation resistance of Grade 92.

The overall irradiation temperatures and doses relevant to this project were reported for different materials including Grade 92, T91, 800H and 800H-TMP [1] [2] [14]. This report includes the result of the ORNL samples, which were irradiated in HFIR. Figure 2 shows the irradiation temperatures and doses for the ORNL samples. In this report, the irradiation temperatures for G92-2b has two ranges, i.e., higher temperature at 683.3°C – ~720°C and lower temperature at 400°C – 496.7°C, while both 800H and 800-TMP are at 580°C.

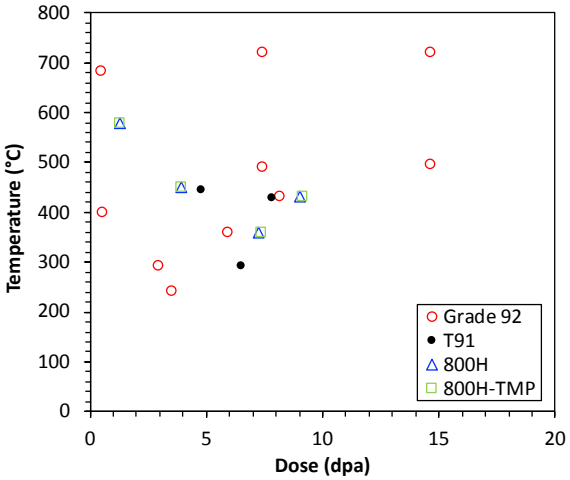

Figure 2. Irradiation temperature and dose conditions of the selected ORNL, LANL, and INL samples.

2.3 SELECTED LANL SAMPLES

A low-temperature-irradiated T91 sample was selected to be compared with NF616 irradiated at a similar temperature. The T91 sample is designated as TA04, irradiated in ATR at ~295°C to ~6.5 dpa. The sample condition is listed in Table 3 and included in Figure 2, together with an unirradiated sample TA#1c. The composition of T91 is listed in Table 4. Both TA04 and TA#1c samples were tensile tested at room temperature, with the results reported by Maloy et al [15]. The samples received at ORNL were hole-punched from the tab section of the tensile-tested samples.

Table 3. Selected LANL samples.

Specimen type	Alloy	Sample ID	Temperature (°C)	Dose (dpa)	Irradiation reactor	Comment
Type SS-J2 tensile	T91	TA04	295	6.5	ATR	Tensile-tested at 25°C [15]
		TA#1c [a]		0		

[a] Unirradiated control sample of the irradiated T91 (i.e. TA04)

Table 4. Composition in weight percent (wt%) of the LANL samples, with Fe as balance.

Alloy	Cr	Ni	Mn	Si	Ti	Al	V	W	Mo	Nb	Cu	C	N	P	S
T91 *	9.22	0.18	0.46	0.24	0.002	0.009	0.24	0.013	0.96	0.063	0.087	0.052	0.057	0.016	0.001

* Also reported 0.002O and 0.021Co. The steel was normalized at 1040°C for 1 h with air cooling and tempered at 760°C for 1 h with air cooling [15].

2.4 SELECTED INL SAMPLES

A total of twelve INL samples of steels 800H, NF616, and T91 were selected, which were irradiated in the ATR of INL through the University of Wisconsin Pilot Project of the ATR National Scientific User Facility [16]. The steels 800H, NF616, and T91 were commercial heats distributed by INL, Japan Atomic Energy

Agency (JAEA), and INL, respectively. The selected samples are listed in Table 5. The samples are in two types: SS-J2 miniature specimens and 3-mm diameter discs.

Table 5. Selected INL samples.

Specimen type	Alloy	Engraved sample code	KGT Num	Temperature (°C)		Dose (dpa)		Dose rate (dpa/s)
				Planned	Average as-run	Planned	As-run total	
Type SS-J2 miniature tensile specimen with 16 × 4 × (<1) mm and gauge 5 × 1.2 × (<1) mm.	800H	N4	1712	400	359	6	7.27	1.30×10^{-7}
		N5	1772	500	451.5	3	3.9	1.35×10^{-7}
		N6	1806	500	431	6	9.01	1.61×10^{-7}
	800H-TMP	P4	2578	400	359	6	7.36	1.31×10^{-7}
		P5	2596	500	451.5	3	3.95	1.37×10^{-7}
		P6	2597	500	431	6	9.12	1.63×10^{-7}
	NF616	D1*	402	300	241	3	3.51	1.29×10^{-7}
		D2	1791	300	291.5	6	2.96	5.29×10^{-8}
		D4	1735	400	359	6	5.91	1.06×10^{-7}
		D6	1783	500	431	6	8.16	1.46×10^{-7}
3-mm diameter disc (~0.2-mm thick)	T91	A4	1729	400	447.5	6	4.78	8.51×10^{-8}
		A6	1790	500	429.5	6	7.79	1.39×10^{-7}

* The sample D1 is at Argonne National Laboratory (ANL), which is to be in-situ tensile-tested during high-energy x-ray diffraction using the Advanced Photon Source (APS) of ANL.

To understand the TMP effect on the mechanical and microstructure response, three samples of 800H-TMP, together with three samples of 800H irradiated in nearly identical conditions, were selected in this project to confirm and elucidate the beneficial effects of GBE/TMP on the neutron irradiation resistance of 800H. The other set of samples includes ferritic-martensitic steels NF616 and T91, classic/typical versions of Grade 92 and 91, respectively. T91 samples are to be used as reference for NF616.

Each sample was engraved with a unique sample code for visual sample identification and assigned with a unique KGT number for sample library record. The information, together with the planned and as-run irradiation temperature and dose listed in Table 5 (included in Figure 2), was obtained from the material library presented online at https://nsuf.inl.gov. The dose rate in Table 5 was deduced from as-run neutron fluence divided by irradiation time. The irradiation conditions, e.g., temperature and dose, will be compared with the analytical reports of the University of Wisconsin Pilot Project [17] [18] [19]. The compositions in weight percent (wt%) of 800H, NF616, and T91 of the INL samples are listed in Table 6 [16]. The compositions are critical for alloy thermodynamic analysis and transmutation analysis to interpret the experimental observations in this project.

Table 6. Compositions in weight percent (wt%) of the INL samples, with Fe as balance*.

Alloy	Cr	Ni	Mn	Si	Ti	Al	V	W	Mo	Nb	Cu	C	N	P	S
800H/800-TMP	20.42	31.59	0.76	0.13	0.57	0.50					0.42	0.069		0.014	0.001
NF616	8.82	0.174	0.45	0.102		0.005	0.194	1.87	0.468	0.064		0.109	0.0474	0.012	0.0032
T91	8.37	0.21	0.45	0.28		0.022	0.216		0.90	0.076	0.17	0.1	0.048	0.009	0.003

* The blank cells are the elements not measured or reported. Oxygen and boron contents were reported as 0.0042% and 0.0017%, respectively, in NF616, which were not reported in the other alloys. 800H was solution-annealed at 1177°C for 24 minutes per centimeter of thickness, followed by a water quench. 800H-TMP was based on 800H, subjected to ~6.6% thickness reduction by rolling at room temperature and then annealed at 1050°C for 1.5 h with water quench. NF616 was normalized at 1070°C for 2 h and tempered at 770°C for 2 h with air cooling. T91 was normalized at 1066°C for 0.8 h and tempered at 790°C for 0.7 h with air cooling.

3. HARDNESS TEST RESULTS

The HFIR-irradiated G92-2b and 800H/800H-TMP, and the ATR-irradiated NF616, T91, and 800H/800H-TMP samples were mechanically polished to a mirror finish for Vickers hardness measurements and microstructural characterization. Vickers hardness measurements were conducted at three levels of loads of 0.1, 0.5, and 1 kgf with three measurements per load. Figure 3a shows the average Vickers hardness with its standard deviation for the control samples and HFIR-irradiated G92-2b samples. For G92-2b, some hardening was shown in the two samples irradiated at lower temperatures, i.e., ~12% hardening of GB03 (0.52 dpa at 400°C) and ~8% hardening of GB04 (7.44 dpa at ~490°C). GB05 has a higher dose of 14.66 dpa but shows ~14% softening due to the longer exposure at the irradiation temperature of 496.7℃. The higher irradiation temperatures (683.3°C to ~720°C) resulted in larger softening of ~8%, ~8%, and ~40% in GB10, GB11, and GB12, respectively.

The Vickers hardness of the HFIR-irradiated 800H (AR2) and 800H-TMP (HG1) and the corresponding references are shown in Figure 3b. Both the AR2 and the HG1 samples show increased hardness after irradiation. The difference between AR2 and HG1 after irradiation is not significant, with slightly lower hardness for sample AR2 after irradiation.

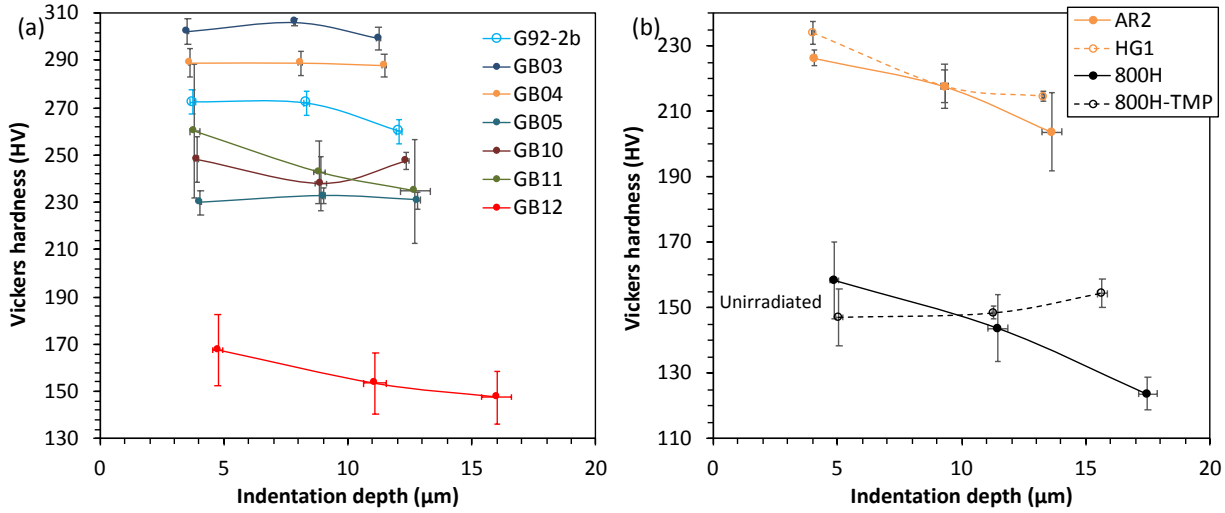

Figure 3. Vickers hardness of the HFIR-irradiated samples of (a) G92-2b (GB03-GB12) and (b) 800H (AR2) and 800H-TMP (HG1).

Figure 4 summarizes the dose-dependent hardness of G92-2b at different irradiation temperature. Hardness is dependent on radiation hardening and radiation-enhanced recovery. Sample GB03, GB04, GB05 were irradiated at the lower temperature range (400℃ - 496.7℃) and they have less recovery effect. Thus, these samples show higher hardness than the GB10, GB11, GB12 that were irradiated at 683.3°C - ~720°C. Although GB05 and GB12 have a larger irradiation dose than the other samples, they have lower hardness than other samples at the similar irradiation temperatures. This indicates a stronger recovery effect than the radiation hardening effect for these samples.

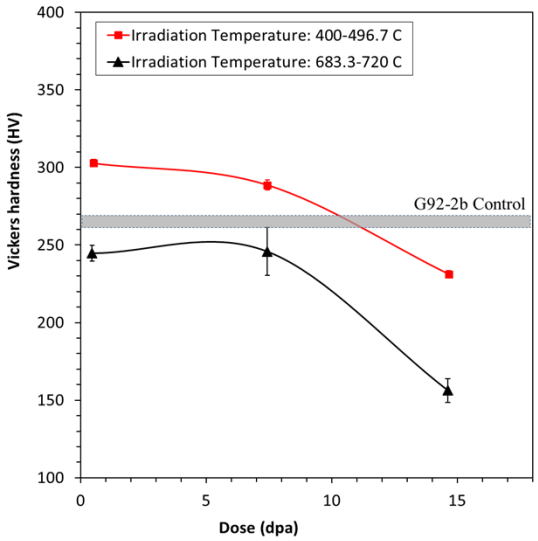

Figure 4. Dose dependence of G92-2b at high and low irradiation temperature.

The Vickers hardness of the ATR-irradiated T91, NF616 and 800H/800H-TMP is shown in Figure **5**. Figure **5**a shows the average Vickers hardness with standard deviation of irradiated NF616 (D2, D4 and D6) and irradiated T91 (A4, A6, and TA04). Compared to the Vickers hardness of unirradiated T91 from literature, which is 210.2 ± 4.2 HV [20], the samples A4, A6, and TA04 showed irradiation induced hardening by ~58%, ~65%, and ~65% respectively. The hardness of unirradiated NF616 is 225 HV from the reference [21], and the samples D2, D4, and D6 increased hardness by ~37%, ~45%, and ~55% respectively.

Figure **5**b shows the Vickers hardness of unirradiated 800H/800H-TMP and the ATR-irradiated 800H (N4, N5, N6) and 800H-TMP (P4, P5, P6). Irradiation induced hardening was observed for both alloys in all the irradiation conditions. The hardness differences between the samples are small considering their standard deviations. Similar to the unirradiated condition, alloy 800H-TMP tended to have slightly higher hardness than alloy 800H in the irradiated conditions. However, the radiation-hardening of alloy 800H-TMP (e.g., ~96±7% to ~107±11%) tended to be slightly smaller than that of alloy 800H (e.g., ~132±15% to 152±10%).

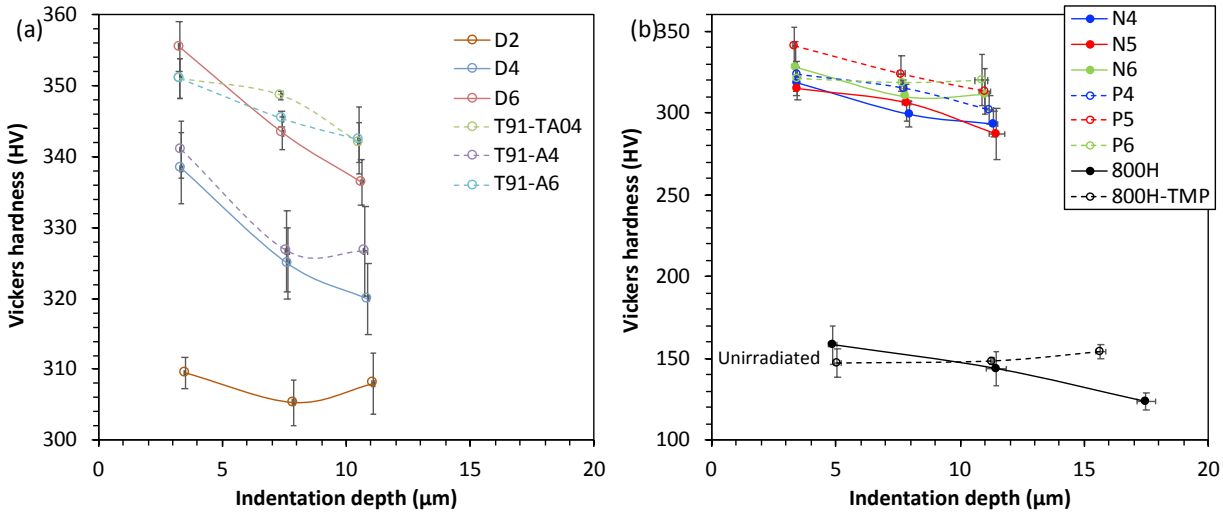

Figure **5**. Vickers hardness of the ATR-irradiated samples of (a) NF616 (D2, D4, D6) and T91 (A4, A6, TA04) and (b) 800H (N4, N5, N6) and 800H-TMP (P4, P5, P6), together with their corresponding references.

4. MICROSTRUCTURAL CHARACTERIZATION

Fractography was performed on the fracture surface of the tensile-tested samples using scanning electron microscopy (SEM) and energy dispersive x-ray spectroscopy (EDS) prior to sample polishing. Microstructure of the samples was characterized using electron backscatter diffraction (EBSD) on the polished samples and transmission electron microscopy (TEM) on electron transparent thin lamellae prepared by focused-ion beam (FIB) for lift-outs from the polished samples.

4.1 FRACTOGRAPHY

Fractography analysis was conducted on the tensile-tested samples of G92-2b, NF616, 800H and 800H-TMP, but not on the disc samples of T91 because of the lack of tensile-tested samples.

4.1.1 HIFR-irradiated G92-2b

Figure 6 shows the fractography of the tensile-tested G92-2b samples, including GB03, GB10, GB11. The tensile tests were conducted at room temperature. GB03 (0.52 dpa) and GB10 (0.46 dpa) that have a similar low dose showed more evident necking than the higher dose sample GB11 (7.44 dpa). GB11 shows large dimples, on the order of a few micrometers. Nb-containing particles were observed inside some of the dimples, and these particles have a size of a few hundred nanometers. The inset of Figure 6f shows examples of Nb-containing particles as pointed by arrows.

Compared with the fractography of samples GB04, GB05, and GB12 that was reported previously [1] [2], GB03, GB04, and GB05 irradiated at 400℃ - 496.7℃ showed evident necking at different doses, while GB10, GB11, and GB12 irradiated at 683.3 - 720℃ showed dose-dependent necking. GB10 (0.46 dpa) showed evident necking, while higher dose samples, especially GB12 (14.66 dpa), did not show significant necking [1] [2]. The fractography result is in agreement with the tensile test results [1] [2], with the ductility of G92-2b maintained up to 14.66 dpa in the irradiation temperature range of 400℃ - 496.7℃, while some loss of ductility (smaller necking and elongation) for higher doses in the higher temperature range of 683.3℃ - 720℃.

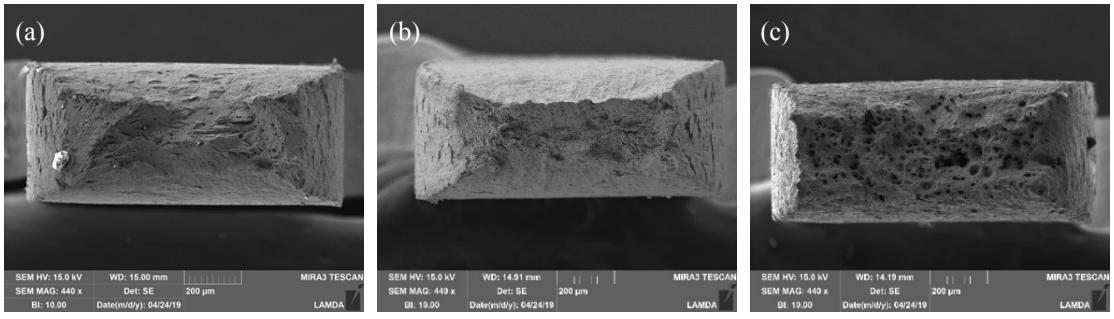

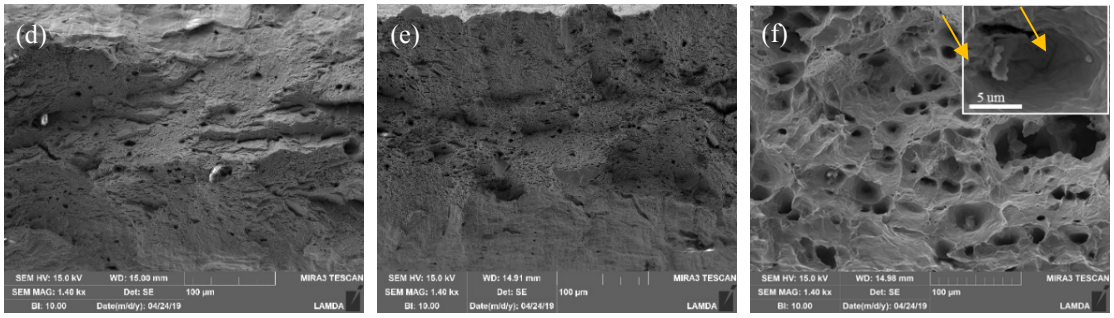

Figure 6. Fractography of the tensile-tested G92-2b samples (a, d) GB03, (b, e) GB10, (c, f) GB11.

4.1.2 HFIR-irradiated 800H/800H-TMP

Figure 7 shows the fractography of the tensile-tested 800H (AR2) and 800H-TMP (HG1). Both samples showed intergranular cracking, with negligible necking. Large grains were observed in both AR2 and HG1, with twin boundaries often seen in the HG1 sample, as shown in Figure 7e. This is in agreement with the thermomechanical processing effect of 800H-TMP that has more twins in the pre-irradiated state. Large TiC particles were observed in a few micrometers at the fracture surface of both samples. $M_{23}C_6$ precipitates were occasionally shown inside the large TiC precipitates, as shown in Figure 7c.

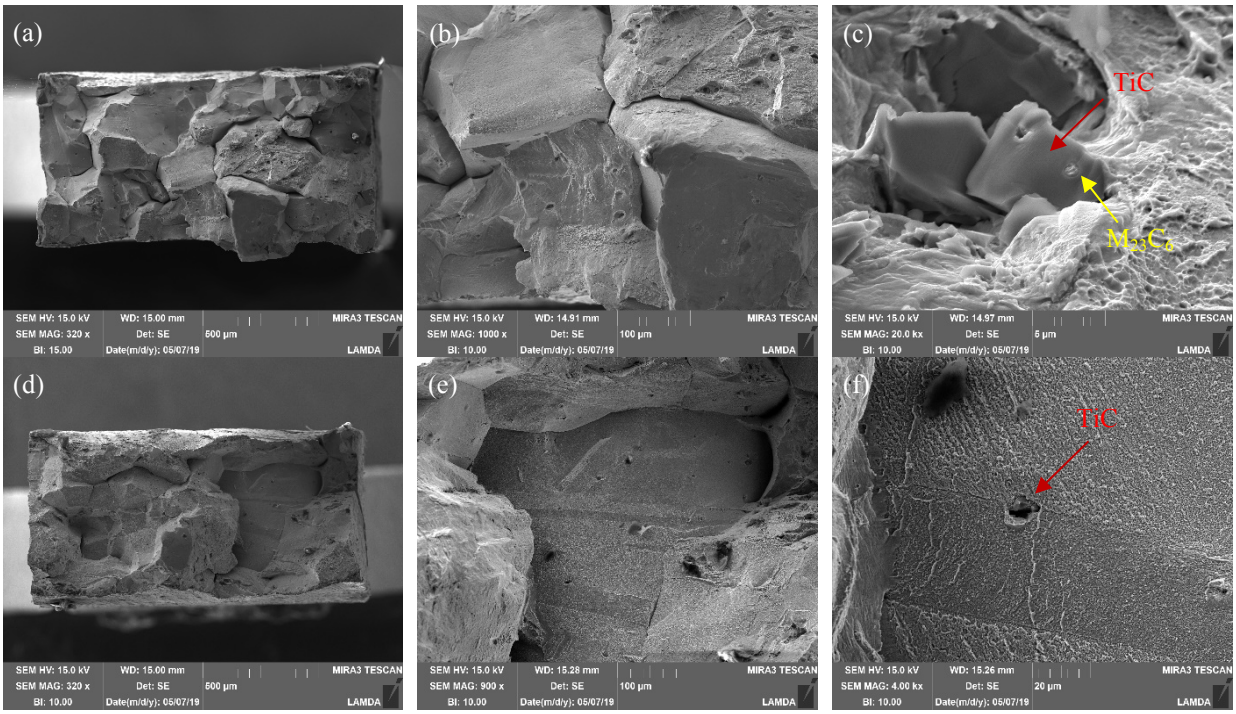

Figure 7. Fractography of the tensile-tested (a, b, c) 800H (AR2) and (d, e, f) 800H-TMP (HG1) samples.

4.1.3 ATR-irradiated NF616

Figure 8 shows the fractography of the tensile-tested NF616 samples D2, D4, and D6. The tensile tests were conducted at room temperature. Sample D2 was irradiated at a lower temperature of 291.5℃, and it showed brittle failure with negligible necking. Cleavage was evident from the fracture surface, where the 'river-like' pattern was dominant, as shown in Figure 8d. Samples D4 and D6 were irradiated at higher temperatures of 359℃ and 431℃, respectively, and both samples showed a ductile failure mode with

obvious necking. Both 'river-like' pattern and dimples were observed on the fracture surface of D4, while dimple features were dominant in sample D6. The Cr-rich particles were observed inside the dimples for both D4 and D6, and they were likely the Cr-rich $M_{23}C_6$ particles. One example of such particles is given in Figure 8f, where $M_{23}C_6$ is marked. This fractography result was in agreement with the tensile test results, where sample D2 failed with a smaller strain than samples D4 and D6 in the tensile tests [3].

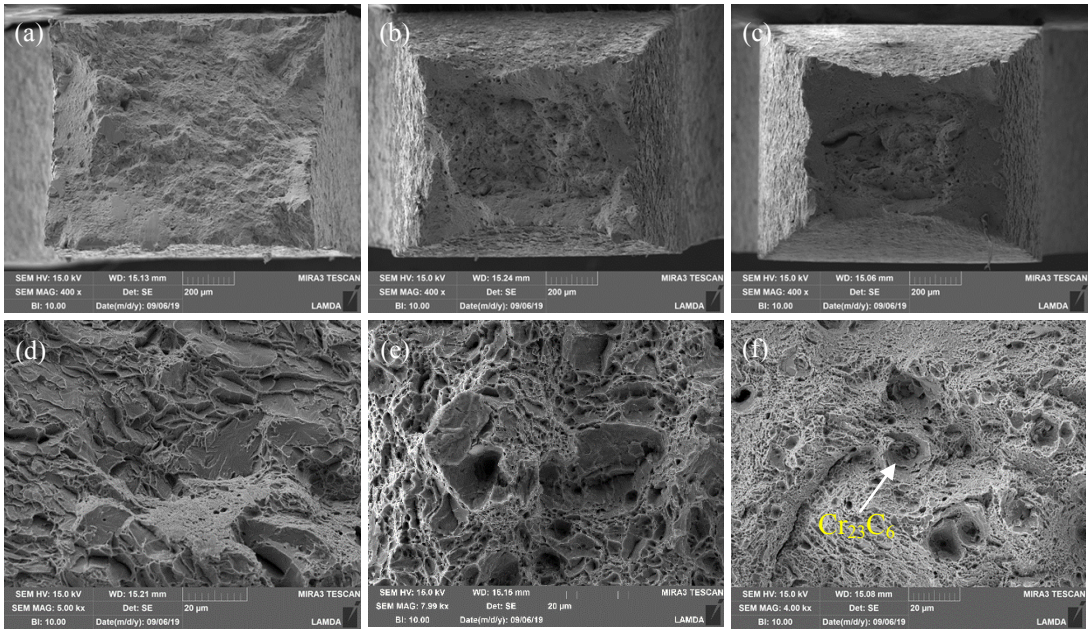

Figure 8. Fractography of the tensile-tested NF616 samples (a, d) D2, (b, e) D4, (c, f) D6.

4.1.4 ATR-irradiated 800H/800H-TMP

Figure 9 shows the fractography of the tensile-tested samples of 800H (N4, N5, and N6) and 800H-TMP (P4, P5, and P6). All tested samples failed in a ductile mode with profound necking. N5 and P5 have a lower irradiation dose and a higher irradiation temperature than the other samples. Their necking is more obvious than the other samples, indicating samples N5 and P5 could be more ductile than the other samples after irradiation. Large Ti-containing particles were observed inside dimples, and the particles had sizes over 5 μm, with two examples of the Ti-containing particles (marked) from samples N5 and P5 shown in Figure 10.

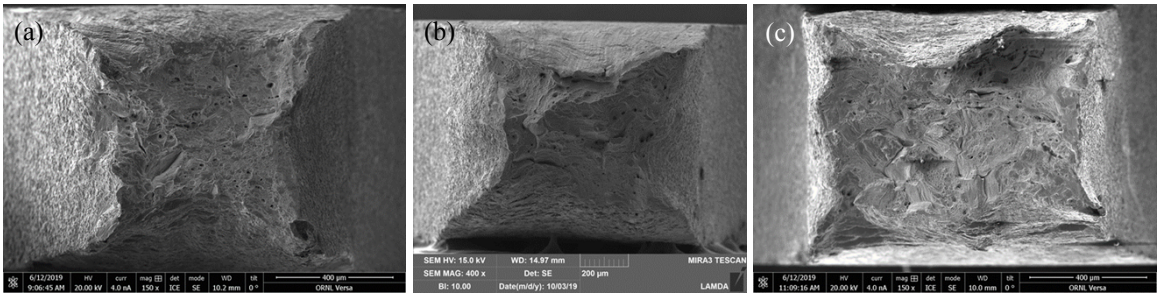

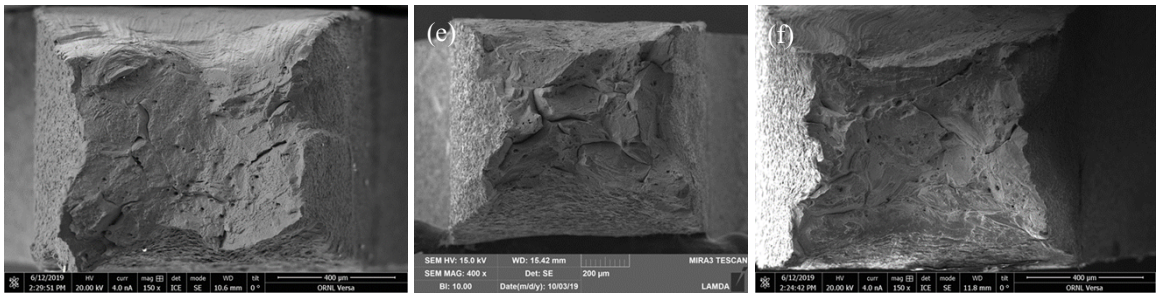

Figure 9. Fractography of the tensile-tested 800H (a) N4, (b) N5, and (c) N6 and 800H-TMP (d) P4, (e) P5, and (f) P6.

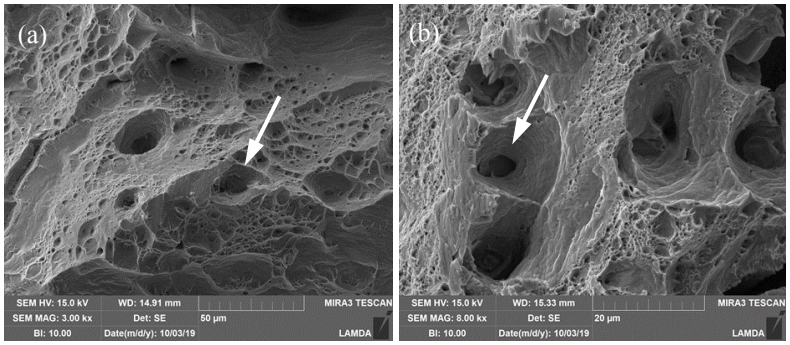

Figure 10. Fractography of tensile-tested (a) 800H (N5) and (b) 800H-TMP (P5) showing the presence of Ti-containing particles inside dimples.

4.2 EBSD RESULTS

EBSD was performed on the archived unirradiated G92-2b and the HFIR-irradiated GB12 (14.63 dpa at ~720°C). Figure 11 shows the EBSD results in inverse pole figure of the two samples at two levels of magnification. The unirradiated G92-2b showed typical martensitic morphology, as shown in Figure 11a and Figure 11b. In contrast, GB12 lost the fine lath martensitic structure after irradiation at ~720℃, which showed coarse approximately equiaxed grain morphology, as shown in Figure 11c. The high magnification map of GB12 in Figure 11d shows that the larger grain is generally consisted of small domains with low angle boundaries.

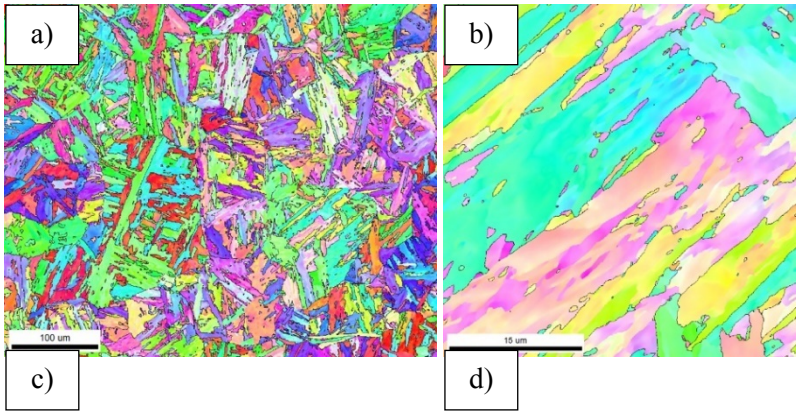

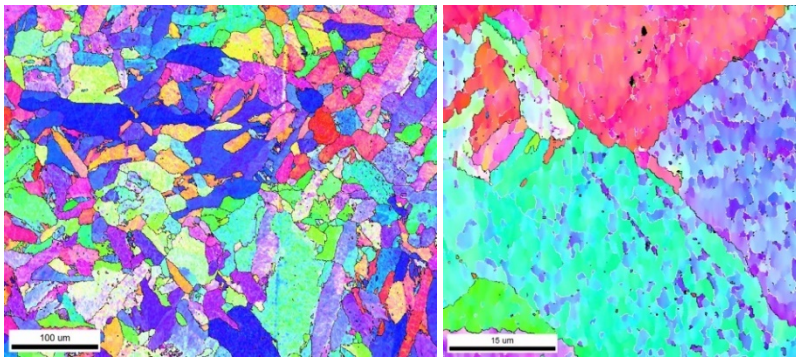

Figure 11. EBSD results of (a, b) archived unirradiated G92-2b and (c, d) HFIR-irradiated G92-2b (GB12).

4.3 TEM RESULTS

4.3.1 Unirradiated G92-2b

Figure 12 shows the microstructure of the unirradiated G92-2b, illustrating a lath structure with width ranging from 100 nm to 400 nm. Precipitates $M_{23}C_6$ (M = Cr primarily) mainly decorated the boundaries, as shown in Figure 12a. The size of $M_{23}C_6$ precipitates was estimated using $\sqrt{LW}$, where L and W are the length and the width of $M_{23}C_6$ precipitates. The average size of $M_{23}C_6$ precipitates was 69 ± 25 nm. Figure 12b shows V-rich MX phase platelet precipitates in the matrix. The image was taken under the two-beam condition of g_{200} near [001] zone. In addition, Nb(C,N) precipitates are present inside grains, as pointed in Figure 12c. The Nb(C,N) precipitates have a spherical morphology with a size of about 25 nm. Figure 12d shows the image of dislocation lines under the [001] zone axis. An average density of ~4×10^{14} m^{-2} for the dislocation lines was estimated from multiple images.

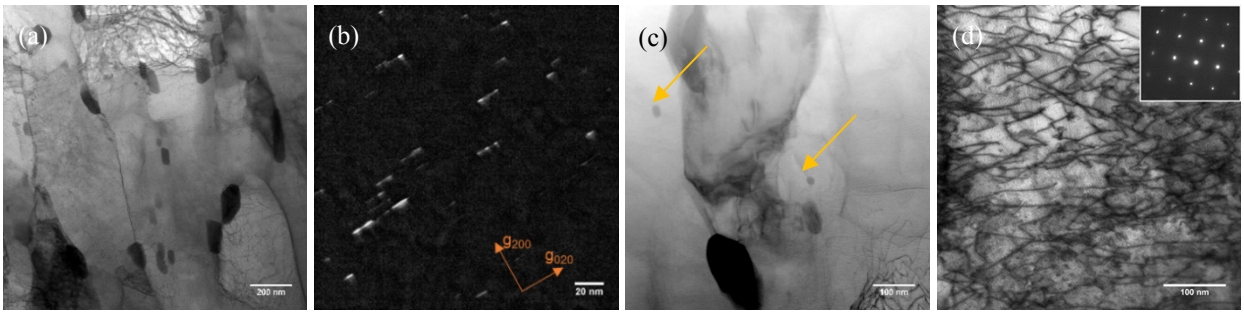

Figure 12. (a, c, d) STEM bright-field images and (b) TEM dark-field image of the unirradiated G92-2b showing (a) $M_{23}C_6$ precipitates, (b) MX precipitates, (c) Nb(C,N) precipitates, and (d) dislocations.

4.3.2 HFIR-irradiated G92-2b – GB03 (0.52dpa, 400℃)

Microstructure was characterized on the tensile-tested irradiated G92-2b at different doses. Figure 13 shows the microstructure of GB03 at the tab section, where it is assumed to be stress free because of the shoulder load during tensile testing. Lath structure seems coarser, with some width over 1 μm as shown in Figure 13a. Further verification will be pursued. $M_{23}C_6$ precipitates decorated boundaries, which have an elongated shape along boundaries as shown in Figure 13b. Spherical Nb(C,N) precipitates are distributed within grains, which have sizes from 20 nm to 30 nm. Figure 13c shows a Nb(C,N) precipitate having a core-shell

structure. The fast Fourier transform (FFT) of the core indicates a [011] zone of Nb(C,N) precipitate in the inset of Figure 13c. The lattice parameter of Nb(C,N) precipitate was measured to be 4.457 ± 0.086 Å. A cluster of precipitates at a grain boundary was also observed, as shown in Figure 13d, which include $M_{23}C_6$ precipitates (pointed by the black arrows), a spherical Nb-rich precipitate (pointed by the orange arrow), and a V-rich precipitate (pointed by the red arrow). Figure 13e shows the dark field image of MX platelet precipitates, similar to the MX in the unirradiated sample in Figure 12b. The dark field image was taken under the two-beam condition of g_{200} near [011] zone. Figure 13f shows the dislocation lines, taken under the [001] zone.

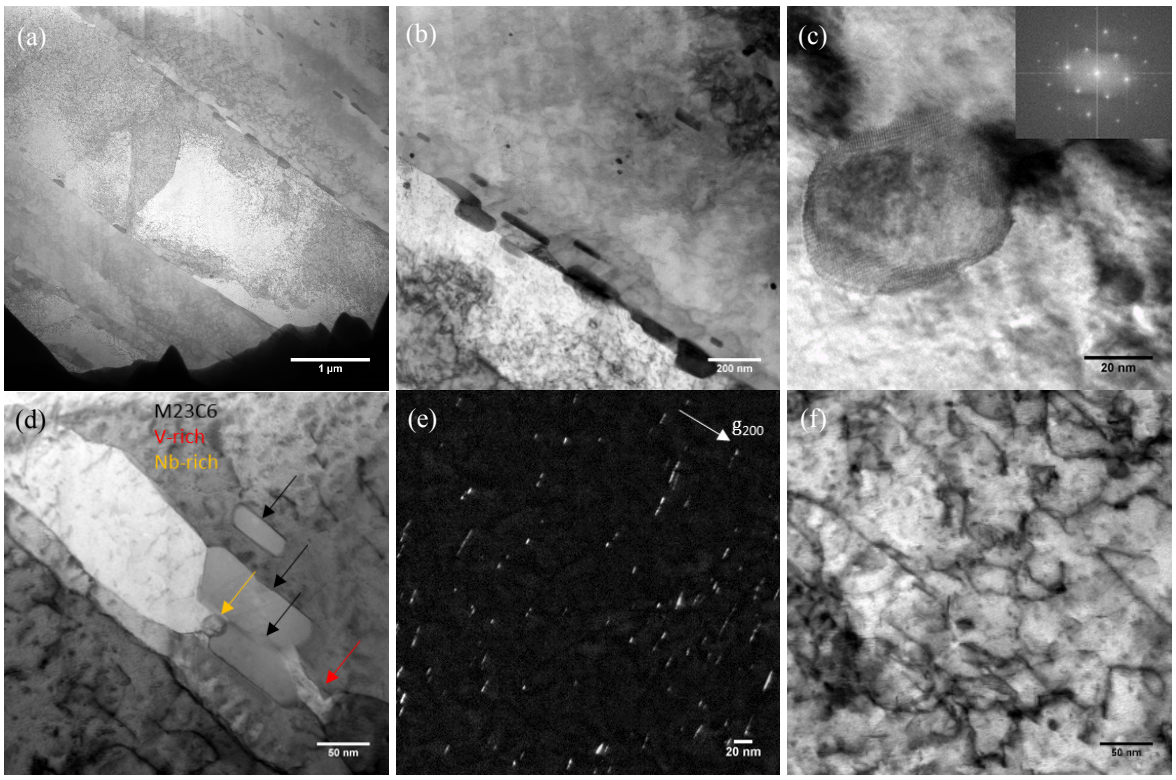

Figure 13. (a, b, c, d, f) STEM bright-field images and (e) TEM dark-field image of GB03 at the tab section.

The microstructure of the gauge section of GB03 is shown in Figure 14. Figure 14a shows the $M_{23}C_6$ precipitates at grain boundaries, as pointed by the blue arrows. Cavities are present and accumulated at the phase boundaries, as pointed by the white arrows in Figure 14a. Figure 14b shows a twinning domain in the center of the image, which has a width of 140 nm. The diffraction patern of the twin is shown in Figure 14c, taken under the [011] zone axis. Multiple precipitates decorated the boundaries beside the twin, including $M_{23}C_6$ precipitates (pointed by the blue arrows), spherical Nb-rich precipitate (pointed by the orange arrow), and V-rich precipitates (pointed by the yellow arrow). The V-rich precipitate was identified by EDS as it does not have strong contrast under STEM.

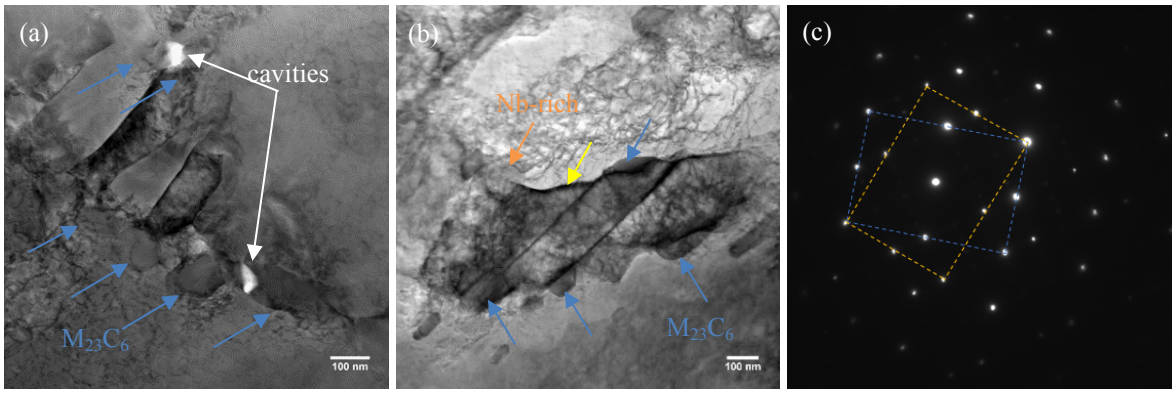

Figure 14. (a, b) STEM bright-field images and (c) the diffraction pattern of the twin in (b) of GB03 at the gauge section.

4.3.3 HFIR-irradiated G92-2b – GB10 (0.46 dpa, 683.3 ℃)

Figure 15 shows the microstructure at the tab section of GB10. Lath structure recovered under the elevated irradiation temperature at 683℃, as shown in Figure 15a, with some laths having a width of ~1 μm. Figure 15b shows the dislocation lines taken under the [111] zone, which shows reduced density than the unirradiated Grade 92 steels. The reduction of dislocation density is attributed to the radiation-enhanced recovery at 683℃. $M_{23}C_6$ precipitates mainly decorated boundaries, as shown in Figure 15c. Some $M_{23}C_6$ precipitates grows into spherical shape at the triple-junction of boundaries, as shown in the Figure 15d. A Laves phase precipitate was also observed, as pointed in Figure 15e. The Laves phase precipitate shows a highly faulted structure adjacent to a $M_{23}C_6$ precipitate at the boundary. Some V-rich precipitates are accumulated at boundaries, which have sizes of ~40 nm and are pointed by the orange arrows in Figure 15f. These precipitates are accumulated at the boundaries of small grains, indicating the pinning effect of V-rich precipitates against grain growth.

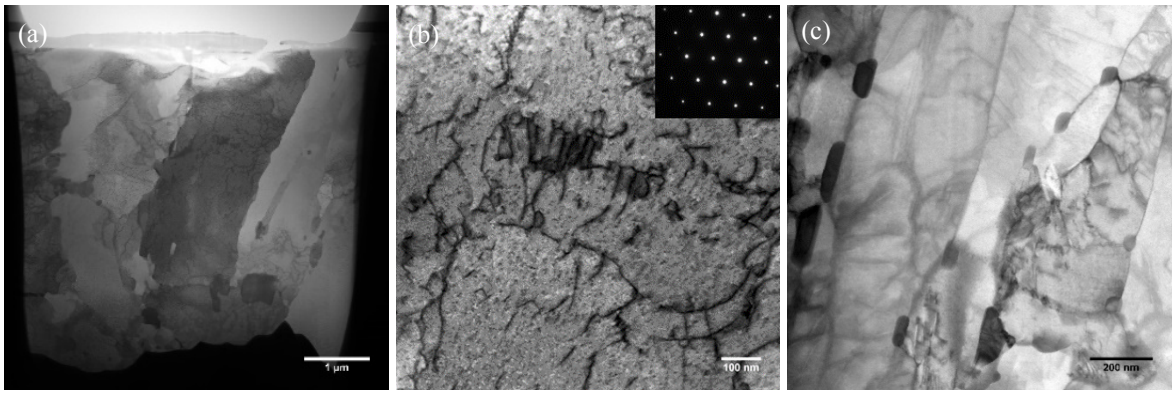

(f)

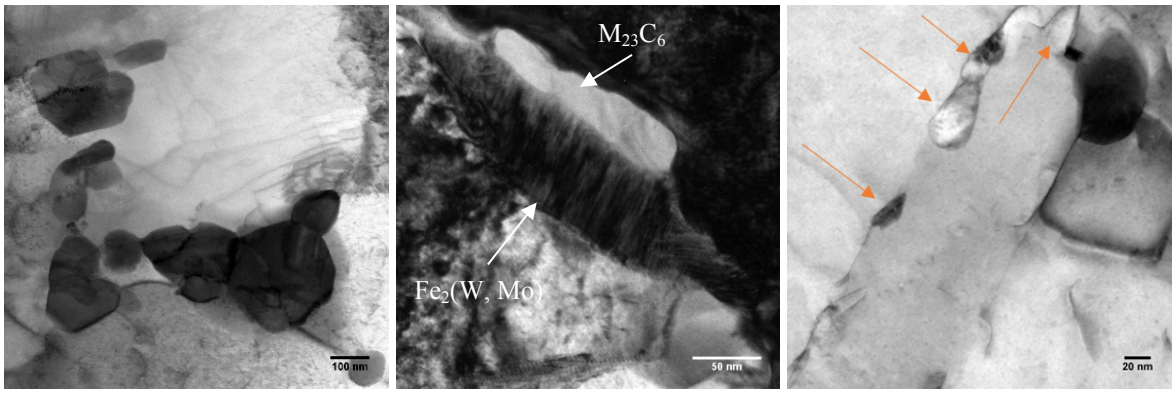

Figure 15. (a, b, c, d, f) STEM bright-field images and (e) TEM bright-field image of GB10 at the tab section, showing (a) overview, (b) dislocation, (c, d) $M_{23}C_6$ precipitates, (e) Laves Phase precipitate, and (f) V-rich precipitates pointed by the orange arrows.

Figure 16 shows the microstructure at the gauge section of GB10, with Figure 16a illustrating the lath structure. Some precipitates were observed at boundaries. Figure 16b shows a cluster of precipitates at a boundary, which includes NbN, $M_{23}C_6$, and MnS precipitates. NbN precipitates have a spherical shape with the diameter of 180nm. The FFT of the NbN precipitate is shown in Figure 16c, which shows an orientation relationship with the matrix of $[011]_{NbN}$ //$[111]_{matrix}$. The lattice parameter of the NbN precipitate was determined to be 4.2571 $\pm$ 0.0857 Angstrom from the FFT. The MnS precipitate with an oval shape is adjacent to the NbN particle with a size of 75 nm. Two $M_{23}C_6$ precipitates were identified, with one of them being amorphous as shown in Figure 16d. Crystalline $M_{23}C_6$ precipitates were also observed, with one of the examples shown in Figure 16e. The diffraction pattern under a [112] zone of $M_{23}C_6$ precipitate is shown as an inset of Figure 16e. The $M_{23}C_6$ precipitate has an orientation relationship with the matrix of $\{111\}_{M23C6}$ // $\{110\}_{Matrix}$. Dislocation lines are evident from the STEM bright field image as shown in Figure 16f, taken under the [001] zone. The density of dislocation lines was measured as 2.5×10^{14} m^{-2}.

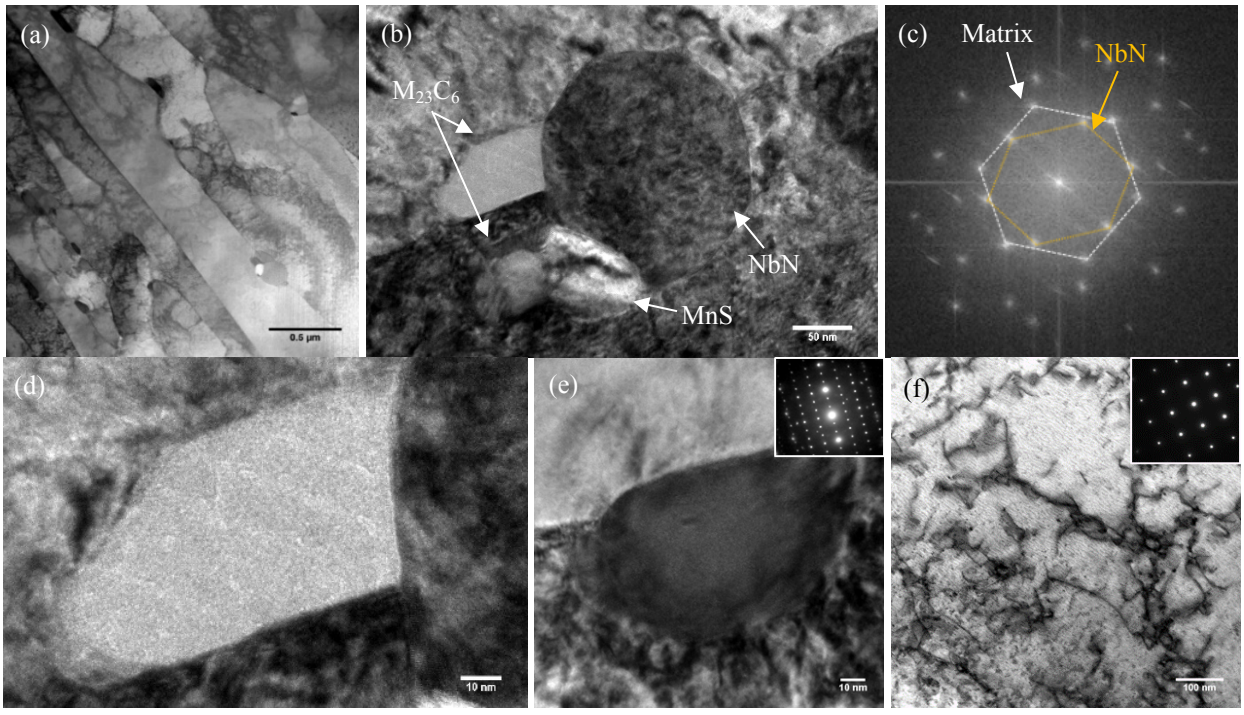

Figure 16**. (a, f) STEM bright-field images, (b, d, e) TEM bright-field images, and (e) the FFT of the NbN precipitate of GB10 at the gauge section.**

4.3.4 HFIR-irradiated G92-2b – GB11 (7.44dpa, ~720℃)

GB11 was irradiated at ~720℃ to 7.44 dpa, and this corresponds to the irradiation time of ~126 days. Equiaxed grain structure is pronounced in the tab section of sample GB11, as shown in the Figure 17a. A few dislocation walls are evident in the top left grain of Figure 17a, which might be the pre-existing packet and block boundaries. Figure 17b shows the dislocation lines under the [001] zone. Voids were observed near dislocation networks, as shown in Figure 17c. Nb-enriched shells were observed around the voids, as shown in the Nb-map in Figure 17d.

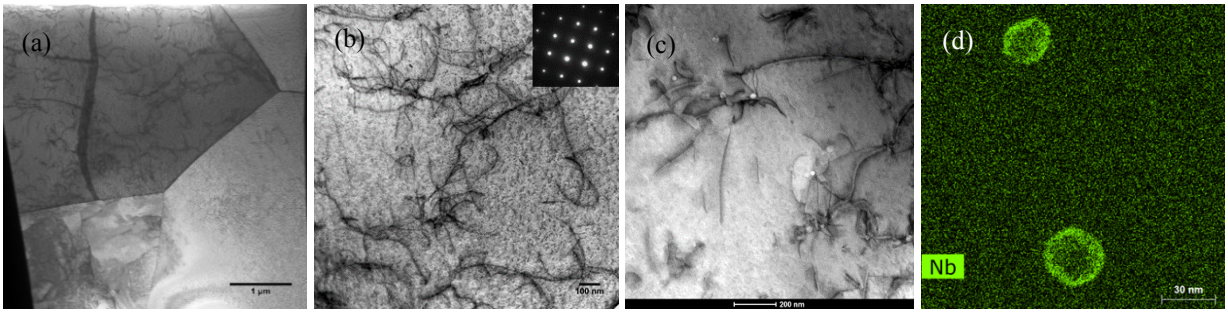

Figure 17. (a, b, c) STEM bright-field images and (d) Nb maps near voids of GB11 at the tab section.

Figure 18 shows the microstructure of GB11 at the gauge section. The TEM foil was lifted out near the fracture site of the tensile specimen, where it had high stress from the tensile test. Dislocation-compiled cells are evident in Figure 18a, with the cell size of hundreds of nanometers. Some dark features accumulated at boundaries, as shown in Figure 18b. The features are shown in the higher magnification image in Figure 18c, which had chemical compositions indistinguishable from the matrix.

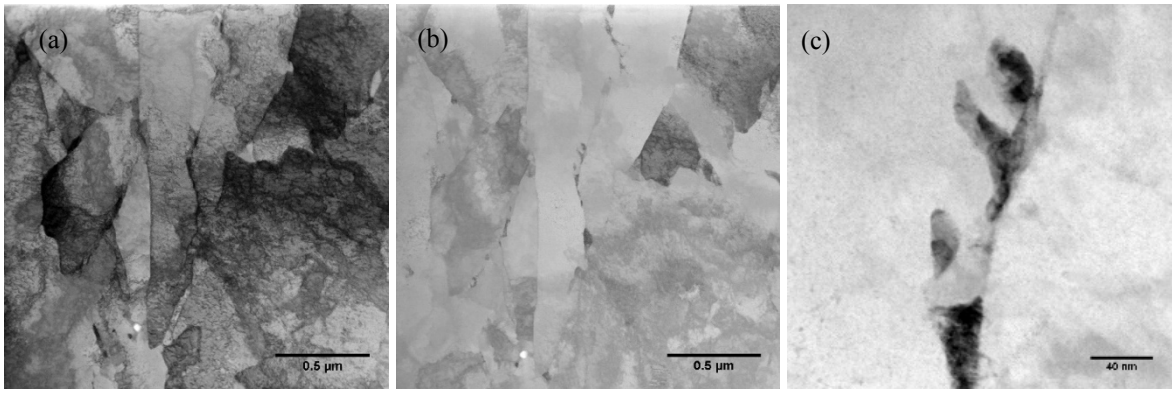

Figure 18**. STEM bright-field image GB11 at the gauge section.**

4.3.5 HFIR-irradiated 800H – AR2 (1.28dpa, 580℃)

Figure 19 shows the microstructure of irradiated 800H sample AR2 at the tab section. Large $M_{23}C_6$ precipitates are accumulated at a grain boundary, and they have sizes of ~110 nm, as shown in the Figure

19a. $M_{23}C_6$ precipitates in smaller sizes are also present inside grains, and they have facet shapes, as shown in the Figure 19b. The diffraction pattern of the $M_{23}C_6$ precipitates with the matrix is shown in Figure 19c, indicating the cube-on-cube orientation relationship of $M_{23}C_6$ precipitates with the matrix. Figure 19d shows the diffraction pattern of the two-beam condition g_{022} near the [011] zone. Diffraction intensities from $M_{23}C_6$ and γ' are observed, which are pointed with orange arrows and a white arrow respectively. This indicates the presence of γ' precipitates in the AR2.

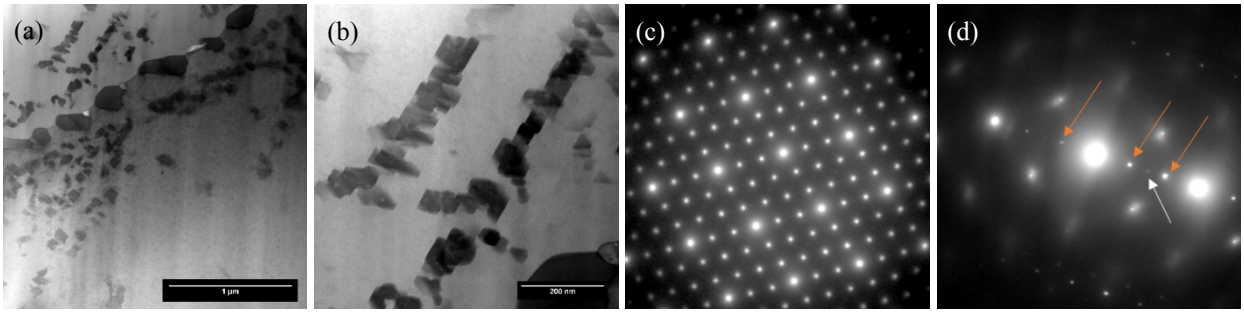

Figure 19. (a,b) STEM bright-field images and (c,d) diffraction patterns at the tab section of 800H (AR2).

The microstructure at the gauge section of sample AR2 is shown in Figure 20. $M_{23}C_6$ precipitates accumulate at a grain boundary as shown in Figure 20a. Dislocation network are evident and shown in Figure 20b. The density of the dislocation network is quantified to be ~1×10^{15} m^{-2}. Dislocation loops are also present, as shown in Figure 20c. The image was taken by the rel-rod method using the two-beam condition g_{311} near the [011] zone, as the diffraction pattern shown on the subset in Figure 20c.

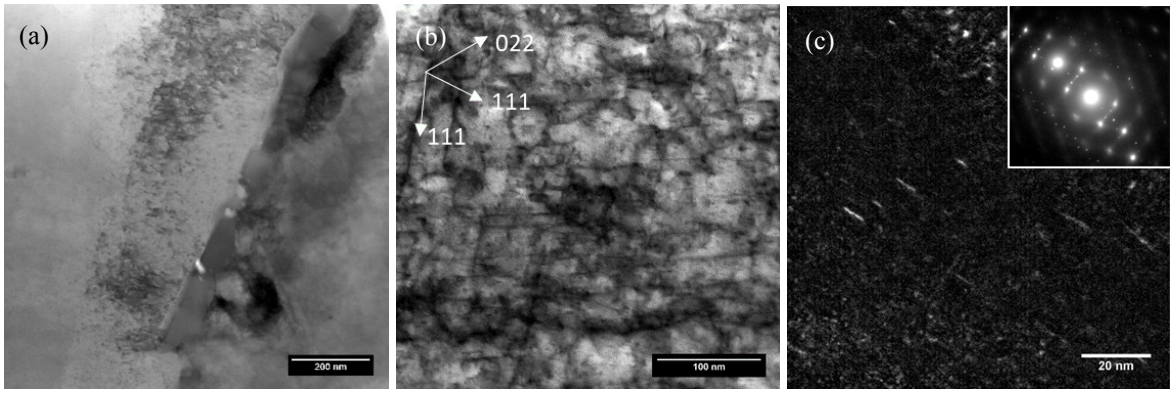

Figure 20. (a,b) STEM bright-field images and (c) dark-field image of the dislocation loops at the gauge section of 800H (AR2).

4.3.6 HFIR-irradiated 800H-TMP – HG1 (1.28dpa, 580℃)

Figure 21 shows the microstructure of irradiated 800H-TMP sample HG1 at the tab section. Large precipitates are accumulated at grain boundaries, as shown in Figure 21a. Dark precipitates are $M_{23}C_6$ (pointed by the orange arrows) that has a size of a few hundred nanometers, with some bright TiC precipitates (pointed by the yellow arrows) embedded inside the $M_{23}C_6$ precipitates. Within the grain, there are some smaller $M_{23}C_6$ precipitates that have a facet shape with a size of about 100 nm as shown in Figure 21b. This indicates that the $M_{23}C_6$ has prefered orientation relationship with the matrix. Figure 21c shows the HRTEM on the interface of the $M_{23}C_6$ precipitate and the matrix. The FFT shown in the inset shows that the precipitate has the cube-on-cube orientation relationship with the matrix. A nano-scale TiC

precipitate exists inside the $M_{23}C_6$ precipitate, which also has the cube-on-cube orientation relationship with the $M_{23}C_6$ precipitate, as indicated by the FFT of the precipitate shown in the inset of Figure 21d. Figure 21e is dark-field image showing the γ' precipitates distribution. The image was taken under a two-beam condition g_{022} near the [011] zone, and the diffraction pattern is shown in the inset of Figure 21e, where diffraction spots of $M_{23}C_6$ and γ' precipitates are pointed by orange and white arrows, respectively. Figure 13f shows the dark-field image of dislocation loops, which was taken under a two-beam condition g_{311} near the [011] zone, and the diffraction pattern is shown in the inset of Figure 13f.

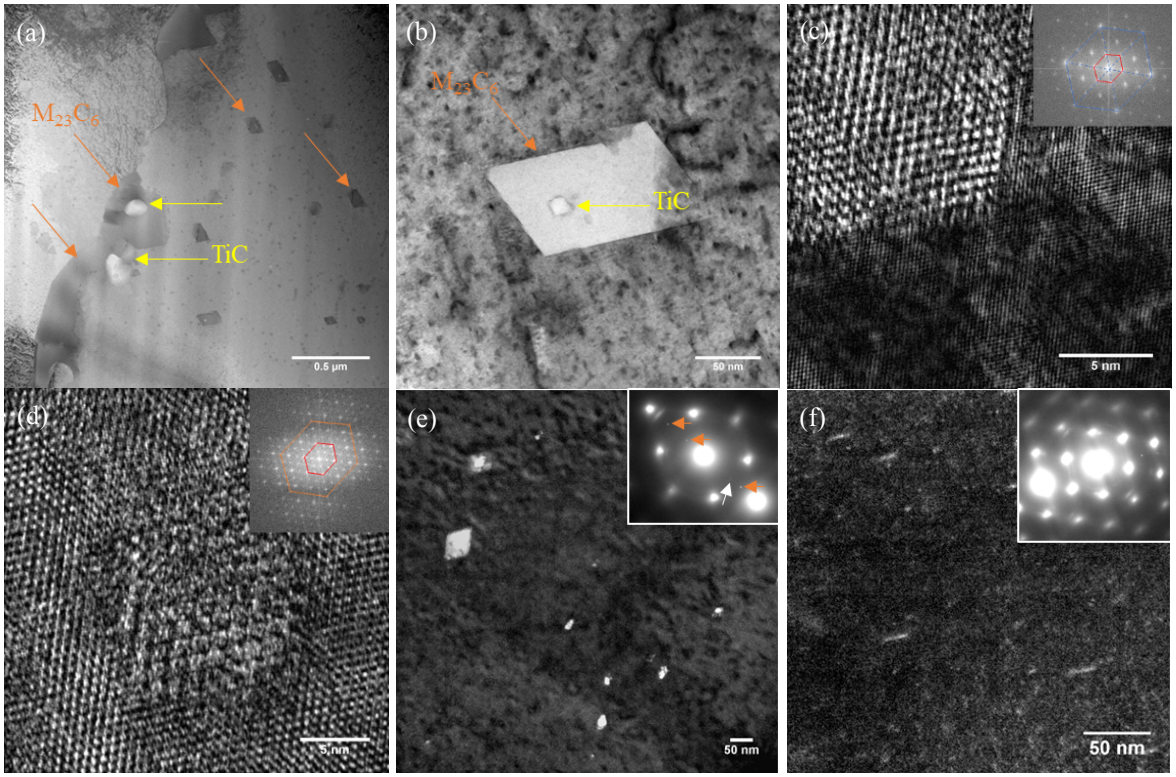

Figure 21. (a, b) STEM bright-field images, (c, d) high-resolution TEM images with FFT as the insets, and (e, f) dark-field images of 800H-TMP (HG1) at the tab section.

Figure 22 shows the microstructure of the HG1 at the gauge section. Precipitates are accumulated at grain boundaries, as shown in Figure 22a. The bright precipitates are TiC particles (pointed by the red arrows), and the dark particles are $M_{23}C_6$ precipitates (pointed by the blue arrows). Unlike the G92-2b samples tested at room temperature, the tensile test of HG1 was conducted at its irradiation temperature of 580°C. It is unclear if the "perfect" alternating alignment of TiC and $M_{23}C_6$ precipitates at the grain boundary was facilitated by boundary migration during the 580°C tensile test. Figure 22b shows the diffraction patterns of matrix under the [001] zone. The secondary diffraction spots are from the γ' precipitates. This shows that the γ' precipitates have the cube-on-cube orientation relationship with the matrix. Figure 22c shows the dark field image of γ' precipitates.

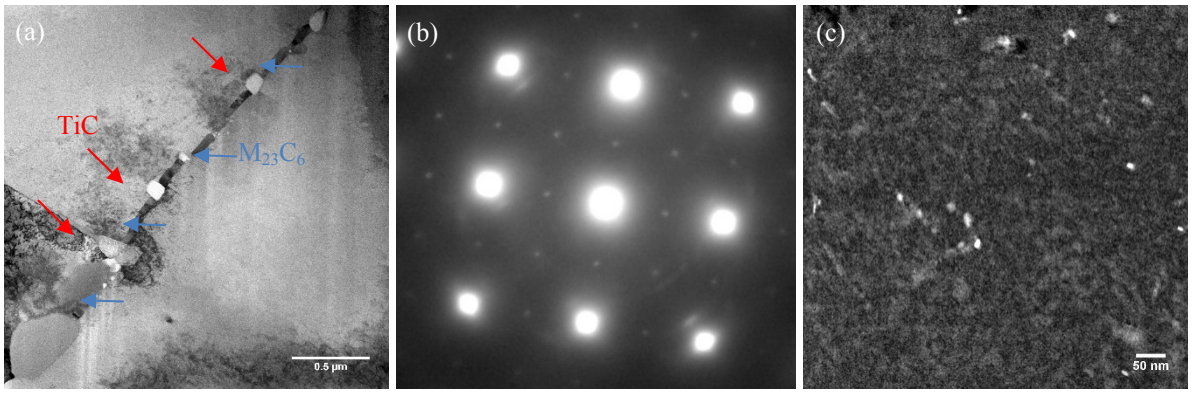

Figure 22. (a) STEM bright-field image, (b) diffraction pattern under the [001] zone, and (c) dark-field image of γ' precipitates of 800H-TMP (HG1) at the gauge section.

4.3.7 Unirradiated T91 – TA#1c

Microstructure of the unirradiated T91 was characterized, with the results shown in Figure 23. Figure 23a shows the overall image of the TA#1c. $M_{23}C_6$ precipitates decorate grain boundaries, as pointed in the Figure 23a. The size of $M_{23}C_6$ precipitates was quantified using $\sqrt{LW}$, where L and W are the length and the width of precipitates. The average size of the precipitates is 68 ± 22 nm. Nanoscale MX precipitates are present, as shown in the dark-field image in Figure 23b. The image was taken under the two-beam condition g_{200} near the [001] zone, as shown in the inset of Figure 23b. The dislocation network is shown in a STEM bright-field image in Figure 23c, taken under the [001] zone, where a few platelet MX precipitates were also observed. .

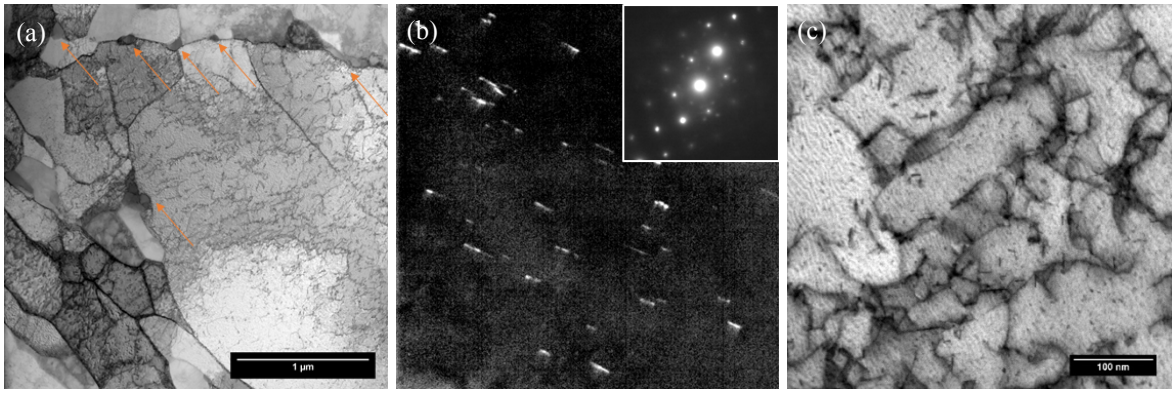

Figure 23. (a, c) STEM bright-field image and (b) dark-field image of MX precipitates of unirradiated T91 (TA#1c).

4.3.8 ATR-irradiated T91 – TA04 (6.5 dpa, 295℃)

The microstructure of the ATR-irradiated TA04 is shown in Figure 24. Figure 24a shows a STEM bright-field image, demonstrating $M_{23}C_6$ precipitates. The average size of $M_{23}C_6$ precipitates was estimated to be 101 ± 40nm, which increased 48.5% in size compared to the unirradiated TA#1c. $M_{23}C_6$ precipitates are accumulated at grain boundaries. Figure 24b shows the region from the dashed box in Figure 24a. Smaller grains are present within the regions where $M_{23}C_6$ precipitates are accumulated, indicating the pinning effect of $M_{23}C_6$ precipitates against the grain growth. Dislocation loops formed in the irradiation environment, as shown in the STEM bright-field image under the [100] zone in Figure 24c. Both {111}- and {100}-type dislocations were observed.

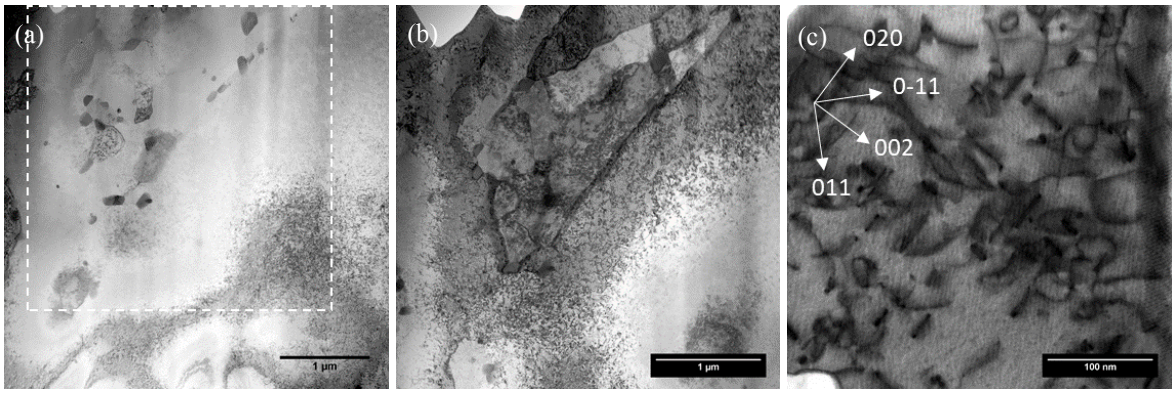

Figure 24. STEM bright-field images showing (a, b) $M_{23}C_6$ precipitates and (c) dislocation loops in the ATR-irradiated T91 (TA04).

4.3.9 ATR-irradiated 800H – N4 (7.27 dpa, 359℃)

Figure 25 shows the microstructure of the tab section of sample N4. Irradiation loops formed, as shown in TEM dark field image in Figure 25a. The dark field image was taken under the two beam g_{311} near the [011] zone. The diffraction pattern of the two-beam condition is shown in the inset in Figure 25a, with only ¼ dislocation loops were shown in the image. Size distribution of dislocation loops was characterized, and most of the loops had sizes ranging from 5nm to 15nm, as shown in the Figure 25b. The average size of dislocation loops was measured to be 12.0 ± 5.0 nm. Nanoscale Si rich clusters were observed, as shown in the Si-map in Figure 25.

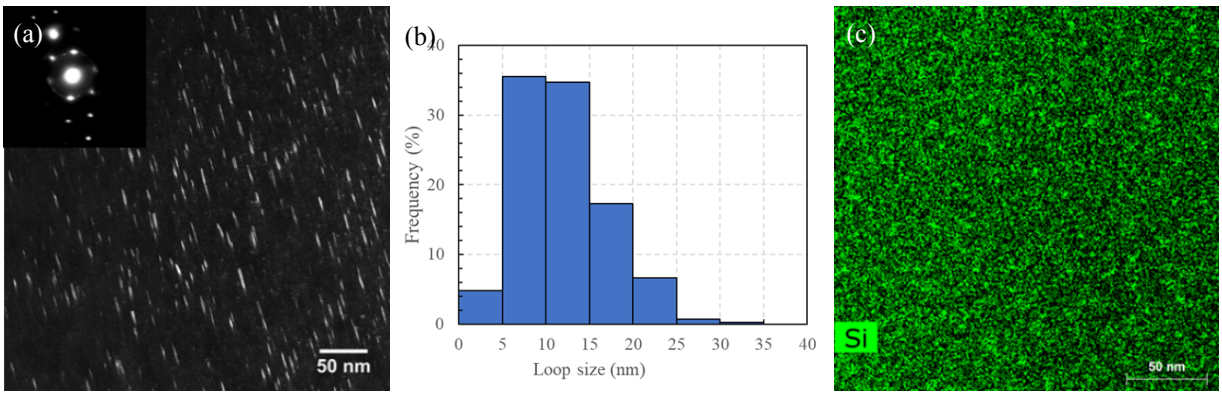

Figure 25. Sample N4: (a) TEM dark-field image of dislocation loops, (b) size distribution of dislocation loops, and (c) Si map.

4.3.10 ATR-irradiated 800H-TMP – P4 (7.36 dpa, 359℃)

Figure 26a shows the overview microstructure image of sample P4. $M_{23}C_6$ (M = primarily Cr) and Ti(C,N) particles were accumulated at grain boundary, as marked in Figure 26a. Other than at grain boundaries, Ti(C,N) were also distributed in the grain interior with smaller sizes, as shown in the Ti map in Figure 26b. Dislocation loops are shown in Figure 26c, taken under the two-beam g_{113} near the [110] zone. The density of dislocation loops was much lower than that in 800H counterpart (see Figure 25a). The size distribution of dislocation loops is shown in Figure 26d, indicating slightly larger sizes than that in sample N4 (see Figure 25b). The average size was measured to be 15.9 ± 7.2 nm. The Si map shown in Figure 26e indicates the presence of the nanoscale clusters.

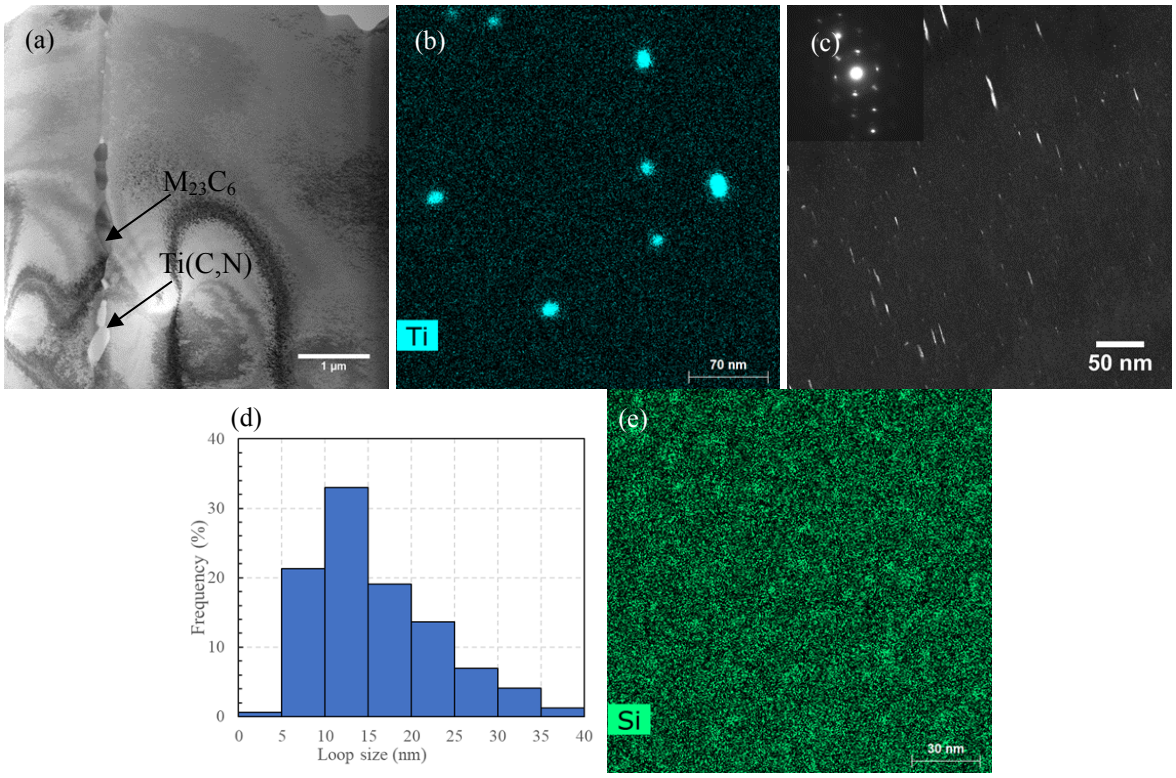

Figure 26. Sample P4: (a) STEM bright-field overview image, (b) Ti map, (c) TEM dark-field image of dislocation loops, (d) size distribution of dislocation loops, and (e) Si map.

4.3.11 ATR-irradiated 800H – N5 (3.9 dpa, 451.5℃)

Figure 27a shows the overview microstructure image of sample N5, demonstrating that the $M_{23}C_6$ precipitates accumulated at a grain boundary. The dislocation loops image is shown in Figure 27b, which was taken under the two-beam g_{311} near the [011] zone as shown in the inset. Size distribution of the dislocation loops was measured and shown in Figure 27c, with the average size of the dislocation loops measured to be 14.1 ± 6.0nm. Nanoscale Si-rich clusters precipitates are present, as shown in the Si map in Figure 27d.

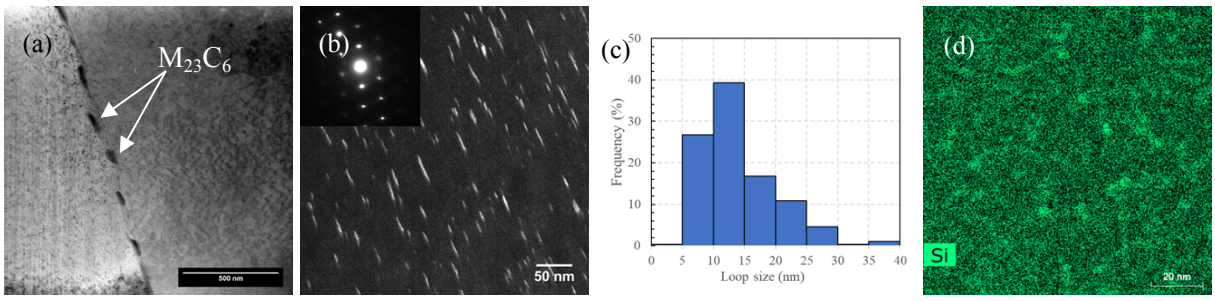

Figure 27. Sample N5: (a) STEM bright-field overview image, (b) TEM dark-field image of dislocation loops, (c) size distribution of dislocation loops, and (d) Si map.

4.3.12 ATR-irradiated 800H-TMP – P5 (3.95 dpa, 451.5℃)

Figure 28a shows the overview microstructure image of sample P5. Both $M_{23}C_6$ and Ti(C,N) precipitates were observed at grain boundaries, as marked in Figure 28a. Small Ti(C,N) precipitates were also observed within the grain, as one of the examples marked. A dislocation loop image is shown in the Figure 28b. Again the dislocation loop density in alloy 800H-TMP (sample P5, see Figure 28b) was lower than that in alloy 800H (sample N5, see Figure 27b) with a similar irradiation condition. Size distribution of dislocation loops was measured, as shown in Figure 28c, and the average size of the dislocation loops was 11.7 ± 5.2 nm. Si map in Figure 28d shows the presence of nanoscale Si-rich clusters in sample P5, although the contrast is less obvious than that in sample N5 (see Figure 27d).

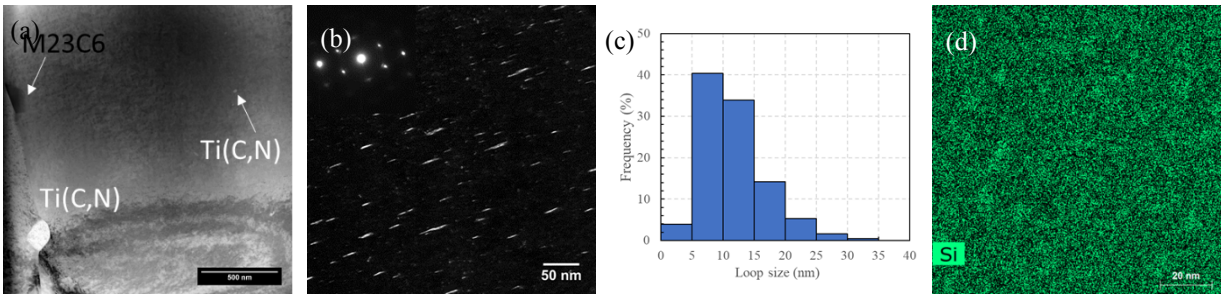

Figure 28. Sample P5: (a) STEM bright-field overview image, (b) TEM dark-field image of dislocation loops, (c) size distribution of dislocation loops, and (d) Si map.

4.3.13 ATR-irradiated 800H – N6 (9.01 dpa, 431℃)

Figure 29a shows the presence of $M_{23}C_6$ precipitates at a grain boundary of sample N6, and the $M_{23}C_6$ precipitates showed the cube-on-cube orientation relationship with the matrix of the left grain, as the diffraction pattern shown in Figure 29b. Dislocation loops were present, as shown in the Figure 29c. The image was taken under the two-beam condition g_{113} near the [110] zone. Size distribution of dislocation loops is shown in Figure 29d, with the average size measured to be 13.9 ± 6.3nm. The Si map in Figure 29e shows the presence of Si rich clusters.

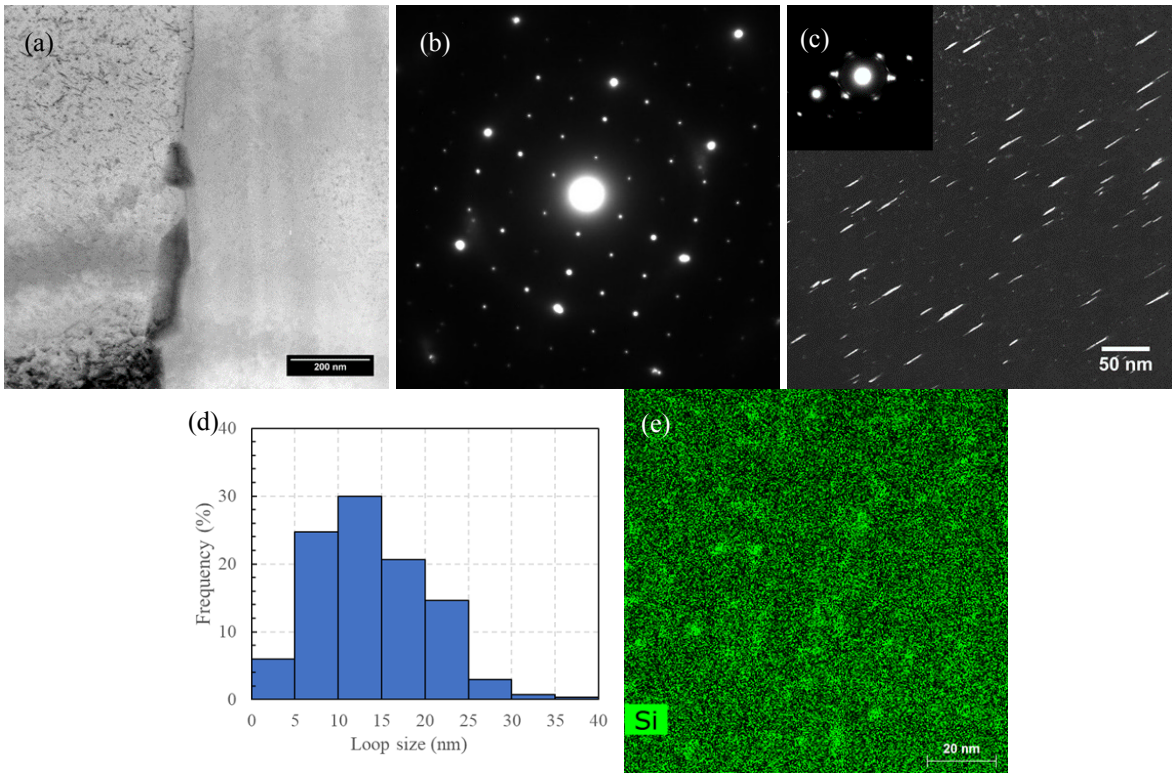

Figure 29. Sample N6: (a) $M_{23}C_6$ precipitate at a grain boundary, (b) diffraction pattern of a $M_{23}C_6$ precipitate with the matrix, (c) TEM dark-field image of dislocation loops, (d) size distribution of dislocation loops , and (e) Si map.

4.3.14 ATR-irradiated 800H-TMP – P6 (9.12 dpa, 431℃)

Figure 30a shows the overview microstructure image of sample P6. A high-angle grain boundary and a twin boundary are shown in the Figure. Many $M_{23}C_6$ and Ti(C,N) precipitates were accumulated at the high-angle grain boundary, while only few Ti(C,N) precipitates was observed at the twin boundary. The diffraction pattern of the twin boundary is shown in Figure 30b, which was taken under the [011] zone. Dislocation loops were present, as shown in Figure 30c. Again, the loop density in alloy 800H (Figure 29c) was higher than that in the TMP version (Figure 30c) of the same irradiation condition. Figure 30d shows the size distribution of the dislocation loops, with the average size measured to be 13.5 ± 5.7 nm. The Si map in the Figure 30e shows the presence of Si rich clusters.

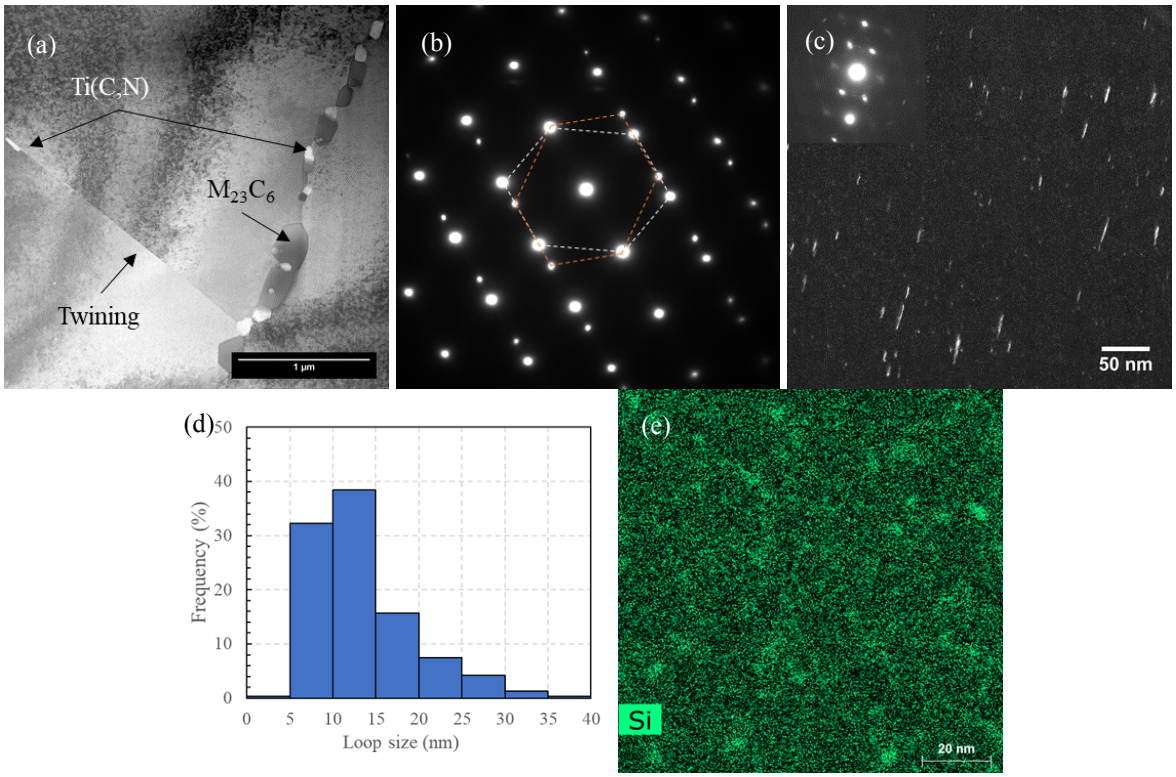

Figure 30. Sample P6: (a) STEM bright-field overview image, (b) diffraction pattern of the twin boundary, (c) TEM dark-field image of dislocation loops, (d) size distribution of dislocation loops, and (e) Si map.

5. CONCLUSION

Ferritic-martensitic steels G92-2b (an optimized Grade 92 heat), NF616, and T91, and austenitic stainless steel 800H and its Grain Boundary Engineering (GBE)-treated version 800H-TMP (ThermoMechanical Processing) were irradiated in the HFIR of ORNL and the ATR of INL. Selected G92-2b samples were irradiated up to 14.66 dpa in the HFIR at two temperature ranges: 400–496.7℃ and 683.3–720℃. NF616 and T91 were irradiated in the ATR up to 8.16 dpa with the irradiation temperatures ranged from 241℃ to 447.5℃. Alloy 800H and 800H-TMP samples were irradiated in both the HFIR and the ATR. Selected 800H and 800H-TMP samples had HFIR irradiation to 1.28 dpa at 580℃ and ATR irradiation up to 9.12 dpa at 359℃ to 431℃. Vickers hardness measurement, fractography, and microstructural characterization were performed on the selected samples in the LAMDA laboratory.

Radiation-hardening of G92-2b was observed at the lower doses and lower irradiation temperatures (400-496.7℃), with GB03 (0.52 dpa at 400℃) and GB04 (7.44 dpa at ~490℃) showing ~12% and ~8% hardening, respectively. Softening by ~14% was observed for GB05 (14.66 dpa at 496.7℃). Radiation-softening of G92-2b was more prevalent at the higher irradiation temperatures (683.3-~720℃), with GB10 (0.46 dpa at 683.3℃), GB11 (7.44 dpa at ~720℃), and GB12 (14.63 dpa at ~720℃) showing ~8%, ~8%, and ~40% softening, respectively. Radiation-hardening of NF616 and T91 was observed with the hardness increased by ~37% to ~65% depending on the irradiation doses and irradiation temperatures. Within the studied irradiation conditions of NF616 and T91, samples with a higher dose had a larger hardness after irradiation. All the tested alloy 800H and 800H-TMP samples in this work showed radiation-hardening by ~96±7% to ~152±10%. Alloy 800H-TMP tended to have slightly smaller radiation-hardening than alloy 800H.

The fractography results of G92-2b sample GB03, GB10, and GB11, together with the previously characterized fractography of GB04, GB05, and GB12, indicated that the ductility of G92-2b was maintained up to 14.66 dpa at the lower irradiation temperatures of 400-496.7℃, while some loss of ductility (less necking) was observed for higher doses at the higher irradiation temperatures of 683.3-720℃. This agrees with the previously reported tensile test results of G92-2b, where the elongation of G92-2b was reduced at higher doses at the higher irradiation temperatures. Dimple sizes increased at higher doses, which are more evident at the higher irradiation temperatures of 683.3-~720℃. The fractography of NF616 sample D2 (2.96 dpa at 291.5℃), D4 (5.91 dpa at 359℃), and D6 (8.16 dpa at 431℃) indicated loss of ductility with negligible necking for sample D2, while ductile failure for samples D4 and D6. Fractography of alloy 800H and 800H-TMP samples in various irradiation conditions showed ductile failure with obvious necking. Dimples were observed, with some of them containing large Ti-rich particles, in all the 800H/800H-TMP samples.

EBSD characterization of GB12 indicated the recovery of the lath structure, which was generally replaced by an equiaxed grain structure. TEM characterization showed the presence of frequent $M_{23}C_6$ (M = primarily Cr), MX (M = primarily V), spherical Nb(C,N) precipitates, and occasional Laves phase precipitates in the G92-2b samples. MX precipitates with sizes of 20-30 nm were observed at boundaries of smaller grains, indicating the pinning effect of the V-rich precipitates. The lath structure recovery was more evident at the higher irradiation temperatures (683.3-~720℃), with decreased densities of line dislocations and $M_{23}C_6$ precipitates. The irradiated T91 (TA04) showed the growth of $M_{23}C_6$ precipitates to 101 ± 40 nm from the initial 68 ± 22 nm in the unirradiated condition. Dislocation loops of both {100} and {111} types were present in TA04. TEM characterization was also performed on the irradiated 800H (N4, N5, N6, and AR2) and 800H-TMP (P4, P5, P6, and HG1). Accumulation of $M_{23}C_6$ precipitates at grain boundaries was observed in all the 800H/800H-TMP samples, and the presence of Ti(C,N) precipitates at grain boundaries and in the matrix was observed in the irradiated 800H-TMP. Some Ti(C,N) precipitates are embedded in the $M_{23}C_6$ precipitates, maintaining specific orientation relationships between

the precipitates and between the precipitate and matrix. In addition, nanoscale Si-rich clusters were observed in the matrix of all the 800H/800H-TMP samples, with the EDS Si maps tending to have a lower contrast in 800H-TMP samples. Atom probe tomography was conducted on the same samples, and their results are being analyzed to be integrated with the TEM results for a confident description of the clusters. Dislocation loops also formed in all the 800H/800H-TMP samples. The density and the average size of dislocation loops were quantified to be in the order of $10^{22} – 10^{23}$ m^{-3} and 11.7 – 15.9 nm, respectively, in the ATR-irradiated 800H/800H-TMP samples. The loop densities in irradiated 800H were higher than that in irradiated 800H-TMP under the same irradiation conditions.

Further systematic data analyses, together with some complementary experiments, will be pursued for these samples to foster peer-reviewed journal article publications.

REFERENCES

[1] L. Tan, "Partial completion of post-irradiation examination of the ORNL samples (No. ORNL/TM-2019/1135)," Oak Ridge National Lab.(ORNL), Oak Ridge, TN (United States)., 2019.

[2] L. Tan, T. Chen, K. Linton, C. Knight and T. A. Saleh, "First annual progress report on the procurement and post-irradiation examination of the selected samples of alloy 800H and Grade 92 and 91 steels (No. ORNL/TM-2019/1136)," Oak Ridge National Lab.(ORNL), Oak Ridge, TN (United States)., 2019.

[3] B. Garrison, W. Zhong, L. Tan and K. Linton, "Tensile Testing and Characterization of Irradiated Grade 92 Ferritic-Martensitic Steels at the IMET Hot Cell and Lambda Facilities," Oak Ridge National Lab.(ORNL), Oak Ridge, TN (United States), 2019.

[4] L. Tan, P. J. Maziasz and T. L. Sham, "Report on the optimization and testing results of advanced ferritic/martensitic alloys. ORNL/TM-2012/288," 2012.

[5] L. Tan and T. Allen, "An electron backscattered diffraction study of grain boundary-engineered INCOLOY alloy 800H," *Metallurgical and Materials Transactions A,* vol. 36, no. 7, pp. 1921-1925, 2005.

[6] L. Tan, T. Allen and J. Busby, "Grain boundary engineering for structure materials of nuclear reactors," *Journal of Nuclear Materials,* vol. 441, no. 1-3, pp. 661-666, 2013.

[7] L. Tan, L. Rakotojaona, T. R. Allen, R. K. Nanstad and J. T. Busby, "Microstructure optimization of austenitic Alloy 800H (Fe–21Cr–32Ni)," *Materials science and engineering: A,* vol. 528, no. 6, pp. 2755-2761, 2011.

[8] L. Tan, K. Sridharan and T. R. Allen, "The effect of grain boundary engineering on the oxidation behavior of INCOLOY alloy 800H in supercritical water," *Journal of Nuclear Materials,* vol. 348, no. 3, pp. 263-271, 2006.

[9] L. Tan, K. Sridharan and T. R. Allen, "Altering corrosion response via grain boundary engineering," *Materials Science Forum,* vol. 595, pp. 409-418, 2008.

[10] L. Tan, K. Sridharan, T. R. Allen, R. K. Nanstad and D. A. McClintock, "Microstructure tailoring for property improvements by grain boundary engineering," *Journal of Nuclear Materials,* vol. 374, no. 1-2, pp. 270-280, 2008.

[11] L. Tan, T. Allen and Y. Yang, "Corrosion behavior of alloy 800H (Fe–21Cr–32Ni) in supercritical water," *Corrosion Science,* vol. 53, no. 2, pp. 703-711, 2011.

[12] R. K. Nanstad, D. A. McClintock, D. T. Hoelzer, L. Tan and T. R. Allen, "High temperature irradiation effects in selected Generation IV structural alloys," *Journal of Nuclear Materials,* vol. 392, no. 2, pp. 331-340, 2009.

[13] L. Tan, J. T. Busby, H. J. Chichester, K. Sridharan and T. R. Allen, "Thermomechanical treatment for improved neutron irradiation resistance of austenitic alloy (Fe–21Cr–32Ni)," *Journal of Nuclear Materials,* vol. 437, no. 1-3, pp. 70-74, 2013.

[14] L. Tan, K. Linton, C. Knight and T. A. Saleh, "Identification and shipment progress of the INL and LANL samples to be received at ORNL (No. ORNL/LTR-2019/1083)," Oak Ridge National Lab.(ORNL), Oak Ridge, TN (United States)., 2019.

[15] S. A. Maloy, T. A. Saleh, O. Anderoglu, T. J. Romero, G. R. Odette, T. Yamamoto, S. Li, J. I. Cole and R. Fielding, "Characterization and comparative analysis of the tensile properties of five tempered martensitic steels and an oxide dispersion strengthened ferritic alloy irradiated at≈ 295° C to≈ 6.5 dpa," *Journal of Nuclear Materials,* vol. 468, pp. 232-239, 2016.

[16] H. J. MacLean, K. Sridharan and T. A. Hyde, "Irradiation Test Plan for the ATR National Scientific User Facility-University of Wisconsin Pilot Project," Idaho National Laboratory (INL), 2008.

[17] K. Davis, J. Rempe, D. Knudson, B. Chase and T. Unruh, "Evaluations of University of Wisconsin Silicon Carbide Temperature Monitors 300 LO and 400 LO B," Idaho National Laboratory (INL), 2011.

[18] S. Wilson, "As-Run Thermal Analysis for the University of Wisconsin Experiment," Engineering Calculations and Analysis Report, 2016.

[19] J. Brookman, "As-Run Physics Analysis for the University of Wisconsin Experiment in the ATR," Engineering Calculations and Analysis Report, 2016.

[20] G. Gupta, Z. Jiao, A. Ham, J. Busby and G. Was, "Microstructural evolution of proton irradiated T91," *Journal of Nuclear Materials,* vol. 351, pp. 162-173, 2006.

[21] J. Jiang, L. Zhu and Y. Wang, "Hardness Variation in P92 Heat-Resistant Steel based on Microstructural Evolution during Creep," *steel research international,* vol. 84, pp. 732-739, 2013.